

APPENDIX III

DETAILS OF CASK RESPONSE TO IMPACT ACCIDENTS

III.1 Finite Element Analysis of the Rail-Steel Cask

III.1.1 Problem statement

Simulate impact of a loaded Rail-Steel cask onto an unyielding surface. Consider impact velocities of 48 kph (30 mph), 97 kph (60 mph), 145 kph (90 mph) and 193 kph (120 mph). Include end, side, and center-of-gravity (cg) over corner impact orientations. Results will be used to assess integrity of the containment boundary and to estimate the extent of any possible breach. Although the deformation and failure of the lid closure bolts is of interest, the ultimate question of containment breach can be determined by assessing the integrity of the inner container. Plastic strains in the stainless steel inner container will be used to predict possible breach of the cask.

III.1.2 Geometric Assumptions and Mesh

A finite element model of the Rail-Steel cask was developed for use with the Sierra Mechanics code Presto. Presto is a nonlinear transient dynamics finite element code developed at Sandia National Laboratories and used extensively for weapons qualification work. The Rail-Steel cask model was developed over several years with many changes along the way to work around limitations in Presto. The model was also required to include the most important geometric features without becoming so large that it couldn't be run on the available computational platforms. The final half-symmetric model consisted of 1.4 million solid hex elements. The drop event lasted approximately 0.5 seconds. The simulation of this drop event required approximately 6-8 days of run time on 256 processors of the Tbird high performance computer at Sandia.

An earlier version of the model used shell elements in areas of thin walled components. The code had difficulty with contact between hexes and embedded shells, and the boundary conditions between the shells and hexes required careful and complicated consideration. Ultimately, the shell elements were replaced by hex elements with 2 or 3 elements through the thickness. Although 2 elements through the thickness is insufficient to correctly predict bending response, these instances were limited to components where bending responses were not considered important. For example, the outer shell of the impact limiter was modeled with 2 hex elements through the thickness. The purpose of this outer layer is to provide constraint to the aluminum honeycomb that comprises the impact limiter. The details of how it bends and folds away from the honeycomb are not important, and not accurate with 2 elements through the thickness. The model details are shown in Figures III-1 to III-4. To allow for internal impacts, gaps were included between the fuel region and the canister and between the canister and the cask interior. Figure III-5 shows the location and magnitude of these gaps.

Comment [A1]: A general description of the casks such as the description in Appendix IV would be helpful to the reader. A statement pointing to the descriptions in Ch 1 and App IV would meet this need.

Comment [A2]: It would be useful to spell out "hexahedral" for this first use of the term.

Comment [A3]: Were the results reviewed for any questionable regions where performance of the impact limiter shell was critical for retaining the honeycomb or protecting it from fire exposure?

Closure bolts were modeled with hex elements, with a minimum of 4 elements across the diameter of the bolt, as shown in Figure III-4.

The total weight of the cask was 364,700 lbs. This weight is high due to an incorrect density value for the aluminum honeycomb that was not discovered until after the runs were completed. The over-weight of the impact limiters results in a more severe loading environment because it increases the amount of kinetic energy that must be absorbed, making all results conservative.

Comment [A4]: Agree that this is conservative.

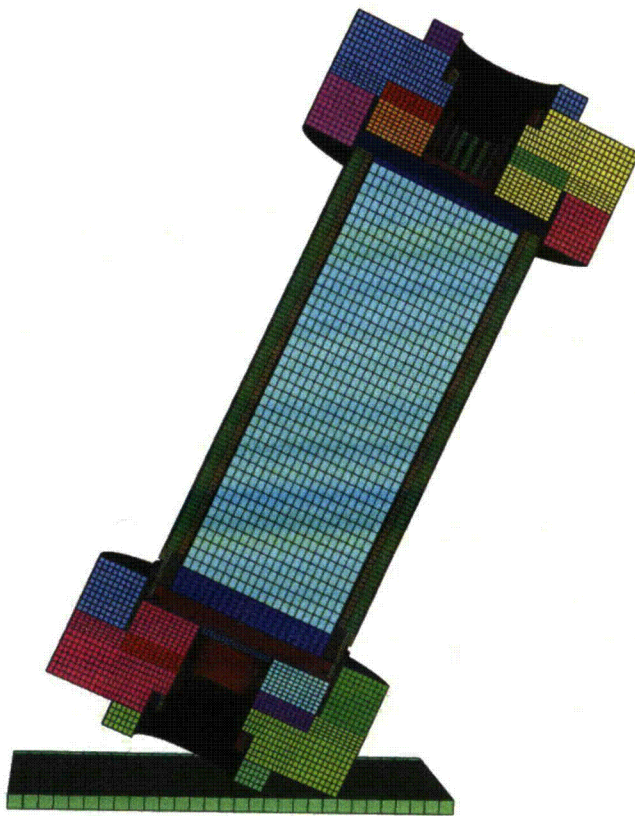


Figure III-1. Half-symmetric mesh of Rail-Steel cask

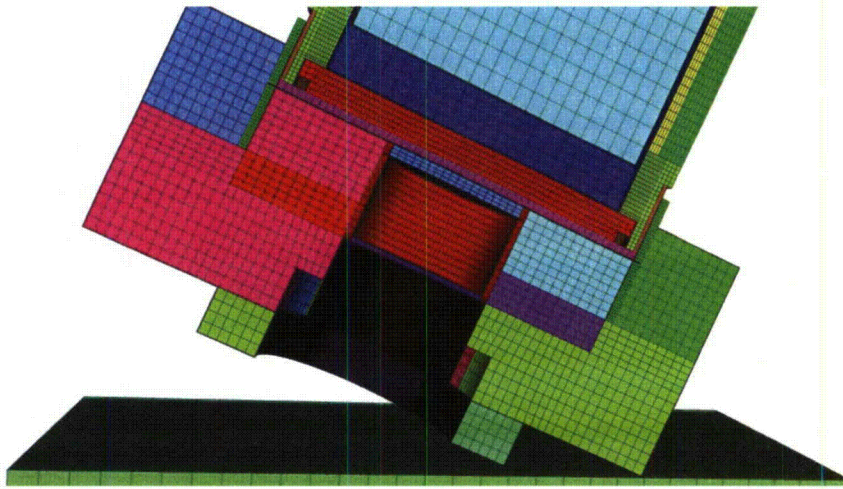


Figure III-2. Impact limiter mesh

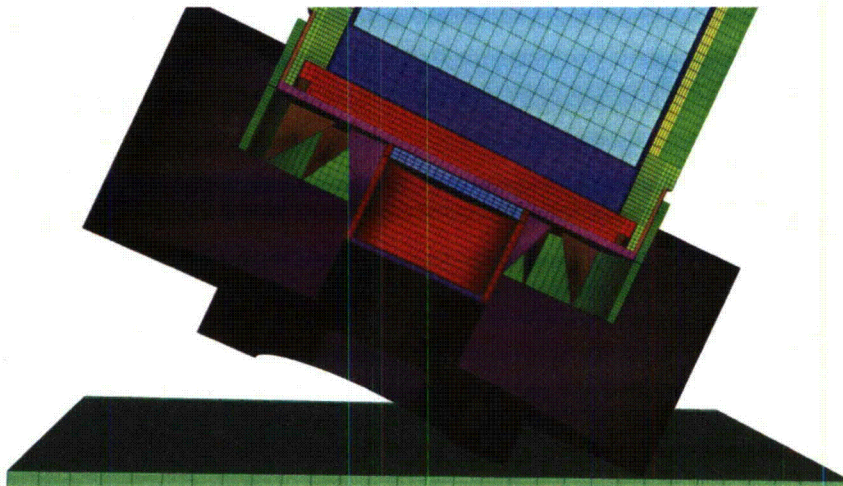


Figure III-3. Impact limiter mesh with honeycomb removed, showing the internal support structure

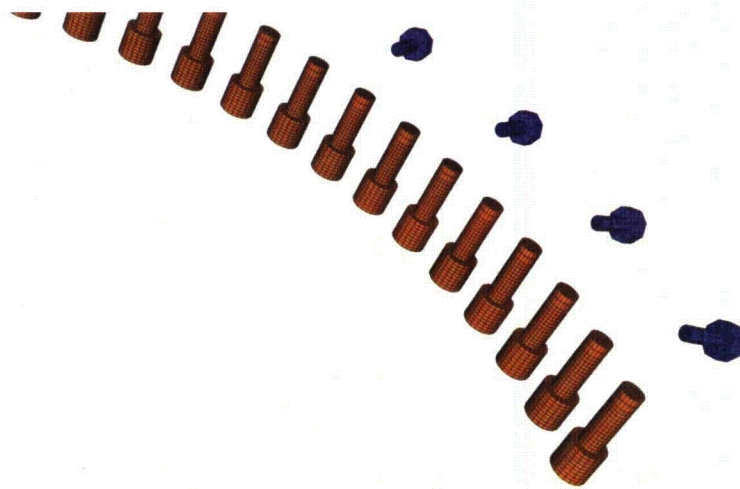


Figure III-4. Mesh of lid closure bolts and impact limiter attachment bolts

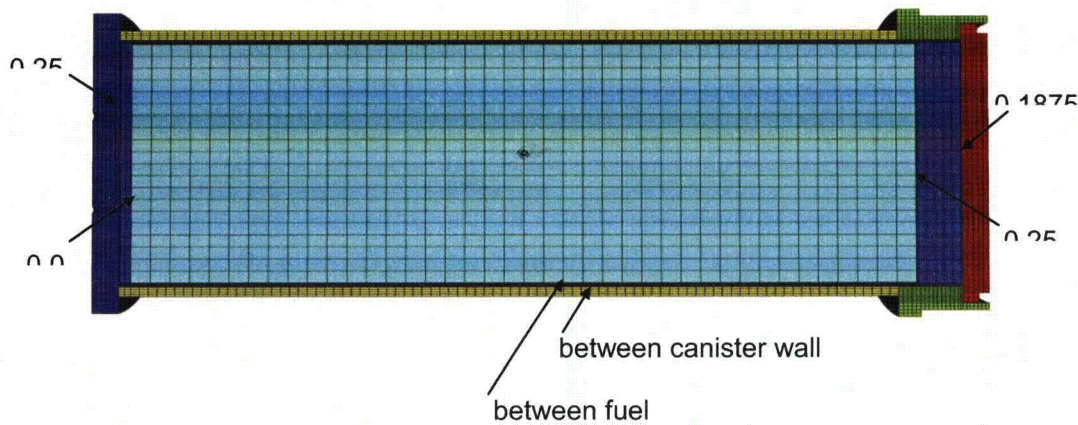


Figure III-5. Locations and magnitudes of internal gaps in the model

The orientation of the model is important to the definition of orthotropic material properties. The cask model is oriented as shown in Figure III-6, and the impact direction is changed for the three impact conditions. For an end drop, the initial velocity is in the +z direction. For a side drop, the

Comment [A5]: Note: Formatting issues with this figure are apparently the result of differences in versions of MS Word.

initial velocity is in the $-x$ direction. And for a c.g. over corner drop, the initial velocity is in a $-0.38269x + 0.92388z$ direction.

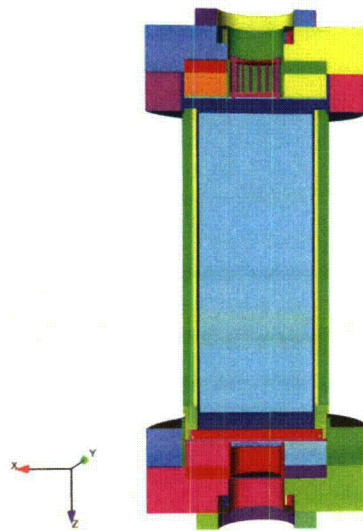


Figure III-6. Orientation of cask model for material property definitions

III.1.3 Material Properties

The response of the closure bolts was of primary importance in these analyses. The threaded ends of the bolts were modeled as fixed into their mating parts using equivalent nodes. The remainder of the bolt was allowed to slide in its through hole. Bolt failure was predicted by considering the equivalent plastic strain (eqps) required for failure. The value of eqps that constitutes failure was assessed using tensile test data and/or references. Details are given below in Section III.1.4.

The aluminum honeycomb in the impact limiters was assumed to be equally strong in the axial and radial directions, and weaker in the circumferential direction. Properties were not varied at 15 degree increments as specified by the design. Instead, properties were defined in the global x-y-z directions and aligned with the loading direction at the point of impact. The honeycomb was modeled with an orthotropic crush material model. The model has been used for many years in Presto and in the commercially available FEM code LSDyna. It is known to behave poorly at the transition to a fully compacted state, when the material transitions from a unidirectional compaction to an isotropic compression with Poisson's expansion. For lower impact velocities

Comment [A6]: There is no discussion of preload in the bolts. Establishment of preload as an initial condition and subsequent evaluation of bolt stress is important and should either be explained or reasons for not considering it should be given. It is worthy of note that the bolt modeling here is much more refined than that employed in earlier published analyses of this cask.

Formatted: Highlight

(30 and 60mph), this was not an issue. However, for the higher impact velocities the model became unstable at material lock-up. To allow the code to continue running, elements that behaved badly were deleted. Since they had already absorbed the energy of the impact and were now just maintaining volume, their deletion was not considered important to the overall cask response.

Material properties are listed below along with the parameters required by Presto(SIERRA, 2009).

Material sa350lf3

Material SA350-LF3 low alloy steel (Holtec, 2001) used for top lid and cask bottom.

Density = 0.00074 lb-s²/in⁴
Material model ep_power_hard
Youngs Modulus = 28.0e6 psi
Poissons Ratio = 0.27
Yield Stress = 37.0e3 psi
Hardening Constant = 192746.0
Hardening Exponent = 0.748190
Luders Strain = 0.0

Material sa230e

Material SA203-E nickel alloy (Klamerus et al., 1996) used for the overpack outer wall.

Density = 0.00074 lb-s²/in⁴
Material model ep_power_hard
Youngs Modulus = 28.0e6 psi
Poissons Ratio = 0.27
Yield Stress = 40.0e3 psi
Hardening Constant = 192746
Hardening Exponent = 0.748190
Luders Strain = 0.0

Comment [A7]: What is the difference between "outer" wall and "external" wall below?

Material sa516gr70

Material SA-516 Grade 70 (Klamerus et al., 1996), used for overpack external wall, buttress plates, and impact limiter gusset plates

Density = 0.00074 lb-s²/in⁴
Material model ep_power_hard
Youngs Modulus = 29.0e06 psi
Poissons Ratio = 0.3
Yield Stress = 53.097e3 psi
Hardening Constant = 0.131331E+06
Hardening Exponent = 0.479290

Comment [A8]: See previous comment with respect to "outer" and "external".

Luders Strain = 0.781E-02

Material testfoam

Material properties taken from typical aluminum honeycomb data as measured at Sandia National Labs (Hinnerichs et al., 2006). Properties used for holtite and impact limiter aluminum cross-ply honeycomb.

Density = 0.0003002 lb-s²/in⁴

Material model orthotropic_crush

Youngs Modulus = 4e6 psi

Poissons Ratio = 0.3

Yield Stress = 40000. psi

Ex = 5.00e04 psi

Ey = 5.00e04 psi

Ez = 5.00e04 psi

Gxy = 2.50e04 psi

Gyz = 2.50e04 psi

Gzx = 2.50e04 psi

Vmin = 0.70

Crush xx = 2300_T

Crush yy = 2300_T

Crush zz = 2300_L

Crush xy = 2300_T

Crush yz = 2300_T

Crush zx = 2300_T

Function 2300_L

0 1415.384615

0.05 2123.076923

0.1 2300

0.4 2300

0.5 1592.307692

0.6 3737.5

0.7 20000

0.9 20000

Function 2300_T

0 1415.384615

0.05 2123.076923

0.1 2300

0.4 2300

0.5 1592.307692

0.6 3737.5

0.7 20000

0.9 20000

Material internals

Used for cask contents inside of inner container.

Density = 0.00029 lb-s²/in⁴
Material model Orthotropic_Crush
Youngs Modulus = 0.5e6 psi
Poissons Ratio = 0.3
Yield Stress = 20000.0 psi
Ex = 0.5e06 psi
Ey = 0.5e06 psi
Ez = 2.2e06 psi
Gxy = 0.25e06 psi
Gyz = 1.1e06 psi
Gzx = 1.1e06 psi
Vmin = 0.70
Crush xx = 2300_T
Crush yy = 700_W
Crush zz = 2300_L
Crush xy = foam_cross_1
Crush yz = foam_cross_2
Crush zx = foam_cross_1

Function foam_cross_1

0 1000
0.6 1000
0.7 10000
0.8 10000

Function foam_cross_2

0 500
0.6 500
0.7 5000
0.8 5000

Material sb637

Material SB637-N07718 (DOD, 199) used for lid closure bolts.

Density = 0.00074 lb-s²/in⁴
Material model m1_ep_fail
Youngs Modulus = 28.6e6
Poissons Ratio = 0.3
Yield Stress = 160000.
Beta = 1.0
Hardening Function = MLEP_Hardening
Youngs Modulus Function = constant_one
Poissons Ratio Function = constant_one
Yield Stress Function = constant_one
Critical Tearing Parameter = 0.13

Critical Crack Opening Strain = 0.01

Material 304ss

Used for the inner welded container (MPC), bottom impact limiter bolts, top impact limiter bolts and shell surrounding impact limiters (Hucek, 1986).

Density = 0.00074 lb-s²/in⁴
Material model ep_power_hard
Youngs Modulus = 53.3e06 psi
Poissons Ratio = 0.3
Yield Stress = 46.246e3 psi
Hardening Constant = 319.05e3
Hardening Exponent = 0.68
Luders Strain = 0.0

Comment [A9]: This is the first time in Ch 3 or App III that the term "inner welded container" is identified as the MPC. It is suggested that the container be identified as the MPC in the text, or, if that is not desired, the designation here be changed as shown.

Formatted: Highlight

Formatted: Highlight

Formatted: Font: 12 pt, Highlight

Comment [A10]: These values of Young's Modulus, Poissons Ratio, and Sy are not consistent with Sec III.2.3 and appear to be set artificially high. This might be justifiable for the impact limiter shell, but would not appear to be for the other components. An explanation for this should be provided.

Formatted: Font: 12 pt, Bold, Italic, Highlight

III.1.4 Criteria for Element Death and Bolt Failure

For all attachment bolts, elements failure is defined according to Presto (SIERRA, 2009) convention.

Criterion is element value of eqps > 1.12
Death on inversion = on

To account for instability in the orthotropic crush material model, elements are removed from the mesh if the following condition occurs, stated in the Presto element death convention.

Criterion is element value of solid_angle <= 0.05
Criterion is max nodal value of velocity(1) > 20000
Criterion is max nodal value of velocity(2) > 20000
Criterion is max nodal value of velocity(3) > 20000
Criterion is max nodal value of velocity(1) < -20000
Criterion is max nodal value of velocity(2) < -20000
Criterion is max nodal value of velocity(3) < -20000
Death on inversion = on

The impact limiter gusset plates and aluminum impact limiter honeycomb are in contact within the impact limiter. The honeycomb would likely fail before the gusset plates in an experiment. Due to the homogenized material modeling of the honeycomb and the relatively coarse mesh, the gusset plates are significantly deformed by the honeycomb. The failure of the gusset plates is defined according to Presto convention.

Criterion is element value of timestep < -0.01
Criterion is element value of volume <= 0.0

Death on inversion = on

III.1.5. Analysis Results

The deformed shape of the cask following each impact analysis is presented below.

Time = 0.05280



Figure III-7. Rail-Steel cask end impact at 193 KPH (120 MPH)

Time = 0.05680

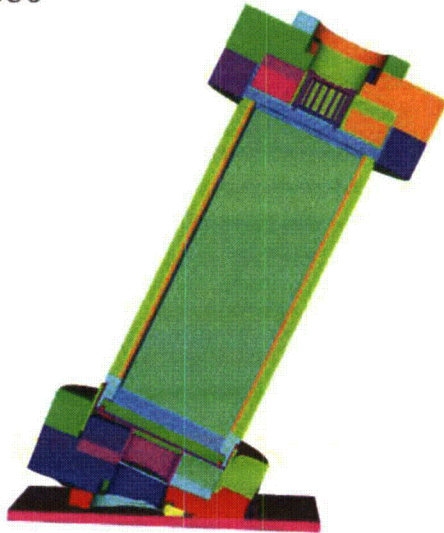


Figure III-8. Rail-Steel cask corner impact at 48 KPH (30 MPH)

Time = 0.06100



Figure III-9. Rail-Steel cask corner impact at 97 KPH (60 MPH)

Time = 0.04960

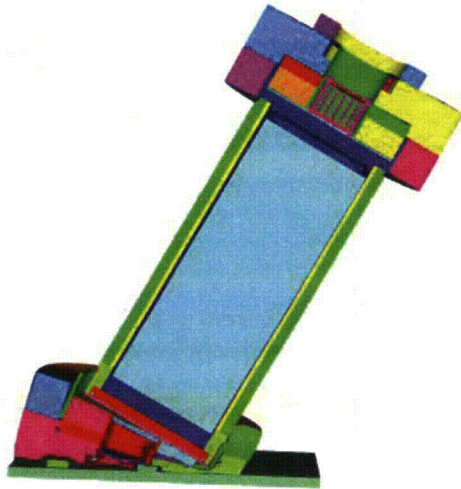


Figure III-10. Rail-Steel cask corner impact at 145 KPH (90 MPH)

Time = 0.03760

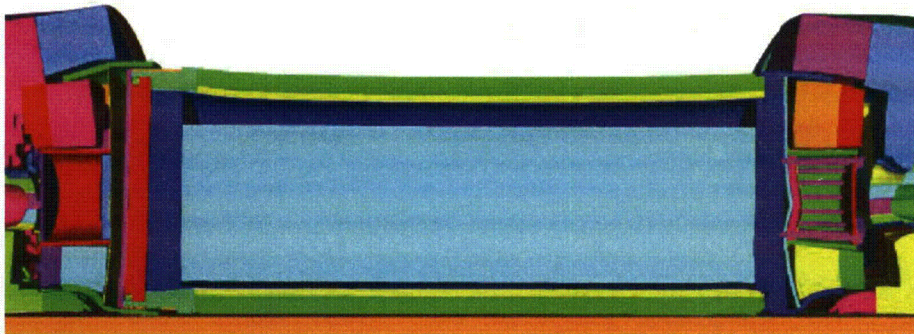


Figure III-11. Rail-Steel cask side impact at 193 KPH (120 MPH)

In the following sections the equivalent plastic strains in the welded inner canister are shown for each analysis case.

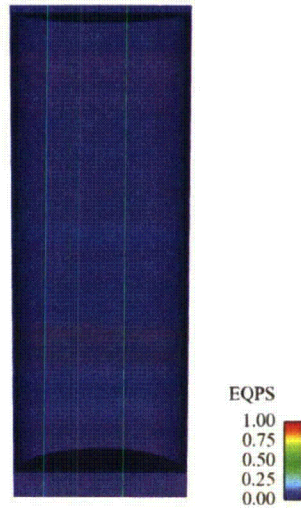


Figure III-12. Plastic strain in the interior welded canister of the Rail-Steel cask from the end impact at 48 KPH (30 MPH)

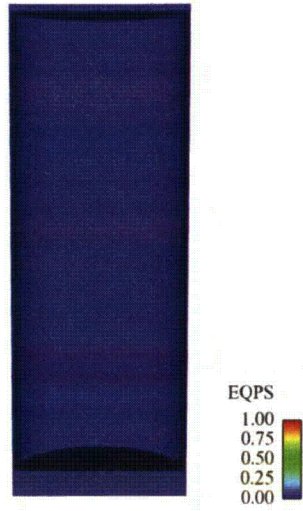


Figure III-13. Plastic strain in the interior welded canister of the Rail-Steel cask from the end impact at 97 KPH (60 MPH)

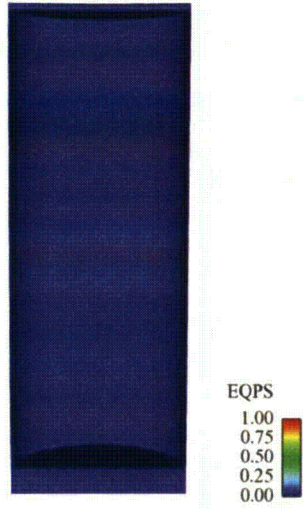


Figure III-14. Plastic strain in the interior welded canister of the Rail-Steel cask from the end impact at 145 KPH (90 MPH)

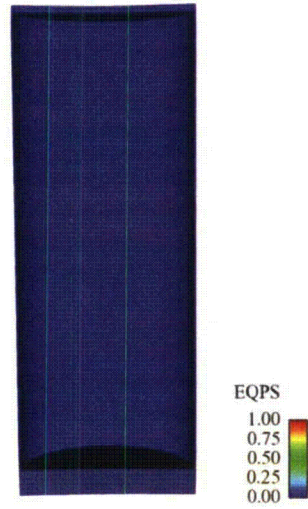


Figure III-15. Plastic strain in the interior welded canister of the Rail-Steel cask from the end impact at 193 KPH (120 MPH)

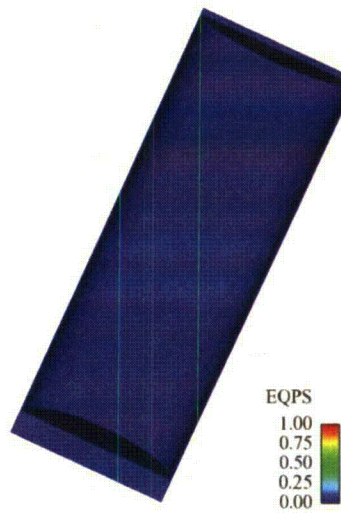


Figure III-16. Plastic strain in the interior welded canister of the Rail-Steel cask from the corner impact at 48 KPH (30 MPH)

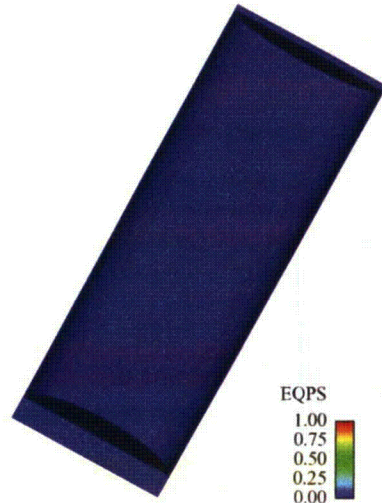


Figure III-17. Plastic strain in the interior welded canister of the Rail-Steel cask from the corner impact at 97 KPH (60 MPH)



Figure III-18. Plastic strain in the interior welded canister of the Rail-Steel cask from the corner impact at 145 KPH (90 MPH)



Figure III-19. Plastic strain in the interior welded canister of the Rail-Steel cask from the corner impact at 193 KPH (120 MPH)



Figure III-20. Plastic strain in the interior welded canister of the Rail-Steel cask from the side impact at 48 KPH (30 MPH)



Figure III-21. Plastic strain in the interior welded canister of the Rail-Steel cask from the side impact at 97 KPH (60 MPH)



Figure III-22. Plastic strain in the interior welded canister of the Rail-Steel cask from the side impact at 145 KPH (90 MPH)

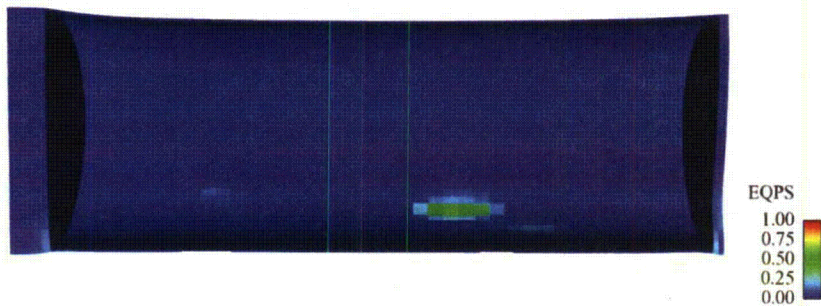


Figure III-23. Plastic strain in the interior welded canister of the Rail-Steel cask from the side impact at 193 KPH (120 MPH)

III.1.6 Acknowledgements

A number of people at Sandia contributed to the development of this model, including Jeff Smith, Bob Kalan, Lili Akin, and Chris Clutz. Nathan Crane was instrumental in resolving execution issues for the model in Presto.

III.2 Finite Element Analysis of the Rail-Lead cask

III.2.1 Problem statement

Simulate impact of a loaded Rail-Lead cask onto an unyielding surface. Consider impact velocities of 48 kph (30 mph), 97 kph (60 mph), 145 kph (90 mph) and 193 kph (120 mph). Include end, side, and c.g. over corner impact orientations. Results will be used to assess integrity of the containment boundary and to estimate the extent of any possible breach. Estimate the deformation and failure of the lid closure bolts and any resulting gap between the lids and the cask. Also estimate the maximum lead slump distance.

III.2.2 Geometric Assumptions and Mesh

A finite element model of the Rail-Lead cask was developed for use with the Sierra Mechanics code Presto(SIERRA, 2009). Presto is a nonlinear transient dynamics finite element code developed at Sandia National Laboratories and used extensively for weapons qualification work. The finite element model was built primarily of hex elements. Shell elements used for the thin stainless steel skin that wraps around the impact limiters. The final half-symmetric model

Comment [A11]: For section III.1.5 of the Appendix to stand alone, the results should be discussed here. At least a statement pointing to the discussion in Chapter 3, Sec 3.2.1, should be provided.

Appendix Section III.1.3 notes that the response of the closure bolts was "of primary importance" in this analysis. Accordingly, results for the closure bolts should be shown or an explanation given. Chapter 3 reports bolt failures, but no graphics or discussion of this is provided here.

For the reader, a tabulation of "g" loads for the various cases would be useful.

Formatted: Font: 12 pt, Highlight

Deleted: finally getting it to run

consisted of 750000 elements. The drop event lasted approximately 0.5 seconds. The simulation of this drop event required approximately 36-60 hours of run time on 64 processors of the RedSky high performance computer at Sandia.

The model details are shown in Figures III-24 to III-27. Unlike the Rail-Steel cask, the basket in the NAC STC completely fills the internal space of the cask. There is the possibility of gaps between the individual fuel elements and the cask lid, but the probability of each of these fuel elements contacting the lid at the same time is very small, so no gap was included in the model.

Closure bolts were modeled with hex elements, with a minimum of 4 elements across the diameter of the bolt, as shown in Figure III-26.

The total weight of the cask was 247300 lbs.

Comment [A12]: The omission of bolt preload should be explained.

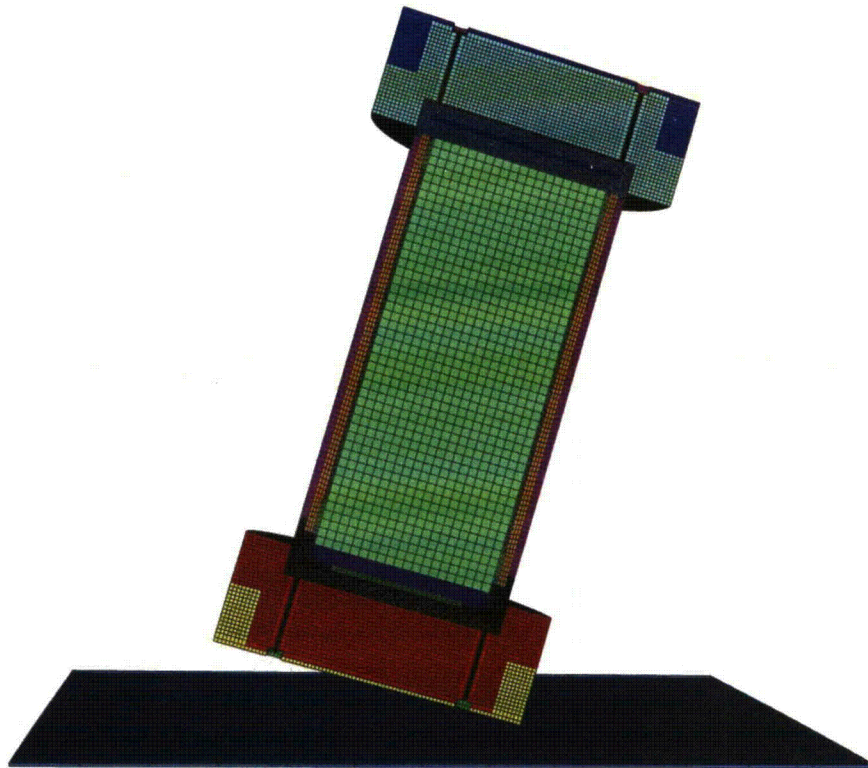


Figure III-24. Half-symmetric mesh of Rail-Lead cask

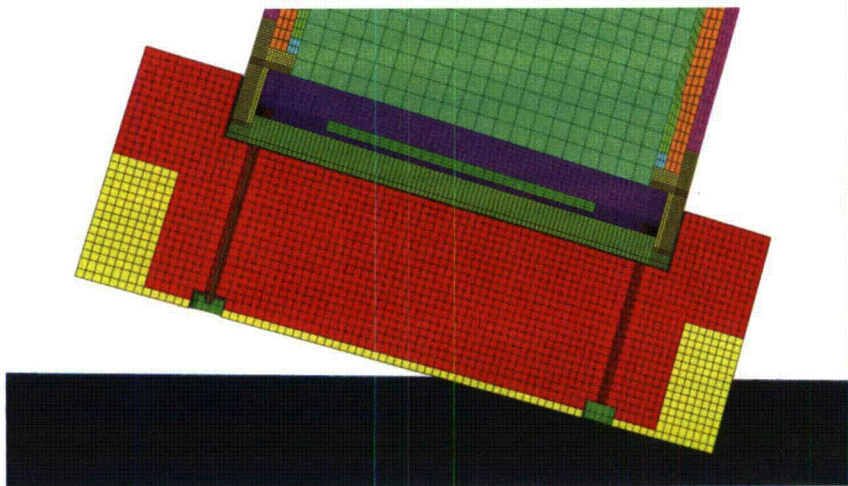


Figure III-25. Impact limiter mesh

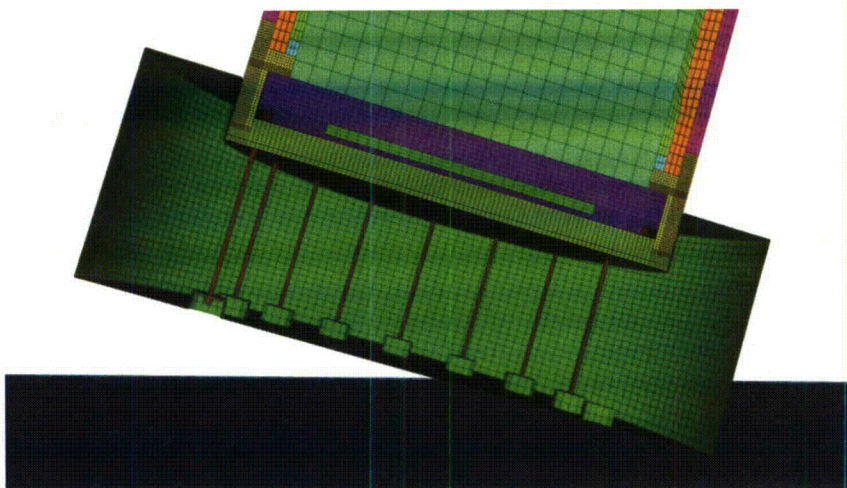


Figure III-26. Impact limiter mesh with wood removed

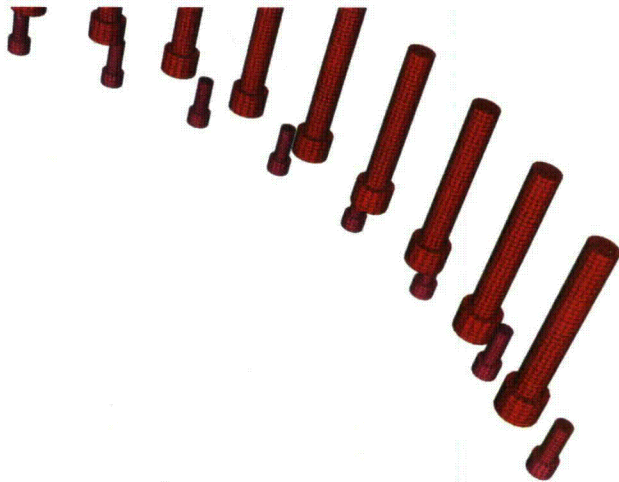


Figure III-27. Mesh of inner and outer lid closure bolts

The orientation of the model is important to the definition of orthotropic material properties. The cask model is oriented as shown in Figure III-27, and the impact direction is changed for the three impact conditions. For an end drop, the initial velocity is in the -y direction. For a side drop, the initial velocity is in the -x direction. And for a c.g. over corner drop, the initial velocity is in a $0.169912x - 0.98546y$ direction.

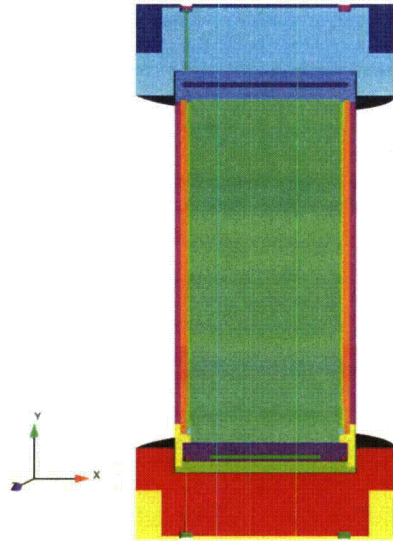


Figure III-28. Orientation of cask model for material property definitions

III.2.3 Material Properties

Material redwood

Used for top and bottom impact limiter

Density = $5.682e-5 \text{ lb-s}^2/\text{in}^4$
 Material model orthotropic_crush
 Young's Modulus = $1.5e6 \text{ psi}$
 Poisson's Ratio = 0.3
 Yield Stress = 20000 psi
 Vmin=0.9
 Ex = $1.5e6 \text{ psi}$
 Ey = $0.3e6 \text{ psi}$
 Ez = $1.5e6 \text{ psi}$
 Gxy = $0.2e6 \text{ psi}$
 Gyz = $0.2e6 \text{ psi}$
 Gzx = $0.2e6 \text{ psi}$
 Crush xx = redwood_strong
 Crush yy = redwood_weak
 Crush zz = redwood_strong
 Crush xy = redwood_shear
 Crush yz = redwood_shear
 Crush zx = redwood_shear

Function redwood_strong
strain stress (psi)

0. 2000.
0.14 4200.
0.28 5100.
0.42 5430.
0.57 6100.
0.71 10100.
0.80 15000.
0.90 20000.

Function redwood_weak
strain stress (psi)

0. 400.
0.14 986.
0.28 1200.
0.42 1275.
0.57 1432.
0.71 2371.
0.80 3521.
0.90 4690.

Function redwood_shear
strain stress (psi)

0.0 1000.
0.60 1000.
0.70 10000.
0.90 10000.

Material balsa

Used for outer corner of top and bottom impact limiters

Density = $1.5e-5 \text{ lb-s}^2/\text{in}^4$

Material model orthotropic_crush

Young's Modulus = $1.5e6 \text{ psi}$

Poisson's Ratio = 0.3

Yield Stress = 20000 psi

Vmin = 0.9

Ex = $1.5e6 \text{ psi}$

Ey = $0.3e6 \text{ psi}$

Ez = $1.5e6 \text{ psi}$

Gxy = $0.2e6 \text{ psi}$

Gyz = $0.2e6 \text{ psi}$

Gzx = $0.2e6 \text{ psi}$

Crush xx = balsa_strong

Crush yy = balsa_weak

Crush zz = balsa_strong

Crush xy = balsa_shear

Crush yz = balsa_shear

Crush zx = balsa_shear

Function balsa_strong
 strain stress (psi)
 0. 2000.
 0.14 4200.
 0.28 5100.
 0.42 5430.
 0.57 6100.
 0.71 10100.
 0.80 15000.
 0.90 20000.

Function balsa_weak
 strain stress (psi)
 0. 400.
 0.14 986.
 0.28 1200.
 0.42 1275.
 0.57 1432.
 0.71 2371.
 0.80 3521.
 0.90 4690.

Function balsa_shear
 strain stress (psi)
 0.0 1000.
 0.60 1000.
 0.70 10000.
 0.90 10000.

Material 304 ss

Properties for 304 stainless steel were obtained from tensile tests conducted at Sandia National Labs.

Elastic values match Rail-Lead SAR (NAC, 2004), but complete response curve is used for placticity.

Used for inner and outer cask wall, shell surrounding impact limiters, and impact limiter attachment bolts.

Density = $7.48e-4 \text{ lb-s}^2/\text{in}^4$
 Material model ml_ep_fail
 Youngs Modulus = $28.0e6 \text{ psi}$
 Poissons Ratio = 0.27
 Yield Stress = $33.0e3 \text{ psi}$
 Beta = 1.0
 Youngs Modulus Function = 304_SS_YM
 Poissons Ratio Function = 304_SS_PR
 Yield stress Function = 304_SS_YS

Hardening Function = 304_SS_H
Critical Tearing Parameter = 7.779
Critical Crack Opening Strain = 0.20

Function 304_SS_H
strain stress (psi)
0.0 0.
0.0395 23.4e3
0.0782 34.9e3
0.1151 45.1e3
0.1509 54.0e3
0.1857 61.7e3
0.2197 68.5e3
0.2527 74.7e3
0.2848 80.5e3
0.3165 86.0e3
0.3470 91.2e3
0.3767 96.4e3
0.4077 101.5e3
0.4378 106.4e3
0.4690 111.4e3
0.5209 119.1e3
0.5797 128.4e3
0.6595 140.6e3
0.7520 156.5e3
0.8639 176.3e3
1.0129 204.2e3
1.2049 242.9e3
1.4476 298.5e3
1.7499 382.8e3
2.1246 519.1e3
2.5960 754.3e3
3.1689 1161.6e3
3.7371 1624.0e3
6.0 3465.5e3

Material filler

Used for internals

Density = 2.92e-4 lb-s²/in⁴
Material model elastic
Youngs Modulus = 122.0e3 psi
Poissons Ratio = 0.30

Material 17 4 ss

Properties for 17-4 stainless steel were obtained from tensile tests conducted at Sandia National Labs.

Elastic values match Rail-Lead SAR (NAC, 2004), but complete response curve is used for plasticity.

Used for outer lid and outer lid bolts.

Density = $7.48e-4$ lb-s²/in⁴
Material model ml_ep_fail
Youngs Modulus = 28.0e6 psi
Poissons Ratio = 0.28
Yield Stress = 100000. psi
Beta = 1.0
Youngs Modulus Function = 304_SS_YM
Poissons Ratio Function = 304_SS_PR
Yield Stress Function = 304_SS_YS
Hardening Function = 17_4_SS_H
Critical Tearing Parameter = 10.0
Critical Crack Opening Strain = 0.20

Function 17_4_SS_H

strain	stress (psi)
0	100000.0
0.00407825	136477.69
0.00879119	153992.02
0.01402863	161193.41
0.01969711	164727.25
0.02677325	166808.60
0.03772328	168627.66
0.12541256	176332.05
0.24107482	183114.13
0.37338829	196318.29
0.51621765	212319.68
0.67105461	234527.78
0.84082846	261327.83
1.03088417	297249.64
1.24626188	344040.44
1.49347177	408459.72
1.78071924	499087.83
2.13871929	625460.64

Material SB637

Material SB-637 Grade N07718 Nickel Alloy Steel (NAC, 2004) used for inner lid bolts

Density = $7.324e-4$ lb-s²/in⁴
Material model elastic_plastic
Youngs Modulus = 2.9e7 psi
Poissons Ratio = 0.32
Yield Stress = 1.508e5
Hardening Modulus = 5.314e5 psi

Beta = 1.0

Material Pb

Lead (Hoffman and Attaway, 1991), used for mid cask wall

Density = 1.06×10^{-3} lb-s²/in⁴
Material model elastic_plastic
Youngs Modulus = 2.0×10^6 psi
Poissons Ratio = 0.3
Yield Stress = 1700. psi
Hardening Modulus = 2000. psi
Beta = 1.

Material ns4fr

Solid synthetic polymer NS-4-FR used for neutron shielding inserts in top and bottom lids

The neutron shielding material was developed by BISCO Products, Inc. and is now supplied by Genden Engineering Services and Construction Company.

NS-4-FR is an epoxy resin that contains boron

Density = 1.571×10^{-4} lb-s²/in⁴
Material model elastic
Youngs Modulus = 5.61×10^5
Poissons Ratio = 0.3

III.2.4 Criteria for Element Death and Bolt Failure

To account for instability in the orthotropic crush material model, elements are removed from the mesh if the following condition occurs, stated in the Presto (SIERRA, 2009) element death convention.

Criterion is max nodal value of velocity(1) > 20000
Criterion is max nodal value of velocity(2) > 20000
Criterion is max nodal value of velocity(3) > 20000
Criterion is max nodal value of velocity(1) < -20000
Criterion is max nodal value of velocity(2) < -20000
Criterion is max nodal value of velocity(3) < -20000
Death on inversion = on

For the impact limiter attachment bolts, elements failure is defined according to Presto convention. This means that failure occurs when the critical tearing parameter (Wellman and Salzbrenner, 1992) is reached, as defined for 304 stainless steel.

Material criterion = ml_ep_fail

Failure of the outer lid and outer lid bolts was defined according to Presto convention when a maximum value of eqps was reached in 17-4 stainless steel. This value of eqps was established

Formatted: Font: 12 pt, Bold, Italic, Highlight

using an analysis of a tensile test specimen, and defining failure at the true strain that corresponds to the true stress approximately midway between the true stress at maximum load and the final true stress. The conservative value was chosen to compensate for the relatively coarse mesh in the bolt.

Criterion is element value of eqps > 1.5

Failure of the inner lid bolts was defined according to Presto convention when a maximum value of eqps was reached in SB-637 Grade N07718 Nickel Alloy Steel.

Criterion is element value of eqps > 0.1

III.2.5 Analysis Results

The deformed shape of the cask following each impact analysis is presented below.

Time = 0.03480



Figure III-29. Rail-Lead cask end impact at 48 KPH (30 MPH)

Time = 0.03480

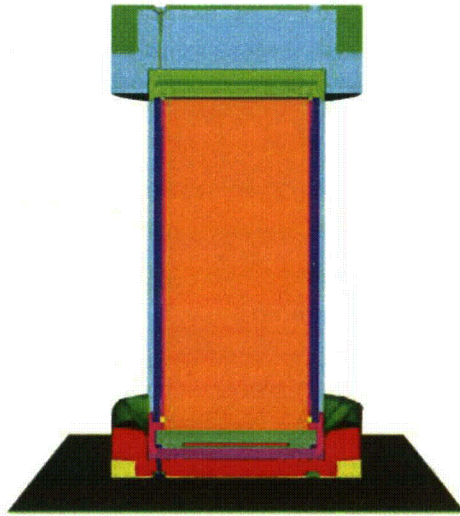


Figure III-30. Rail-Lead cask end impact at 97 KPH (60 MPH)

Time = 0.03480



Figure III-31. Rail-Lead cask end impact at 145 KPH (90 MPH)

Time = 0.03480



Figure III-32. Rail-Lead cask end impact at 193 KPH (120 MPH)

Time = 0.06420

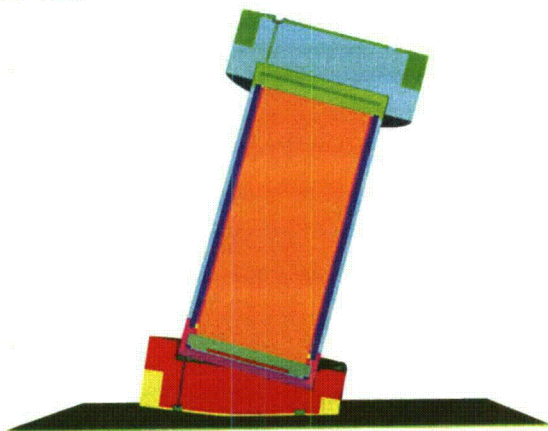


Figure III-33. Rail-Lead cask corner impact at 48 KPH (30 MPH)

Time = 0.05040

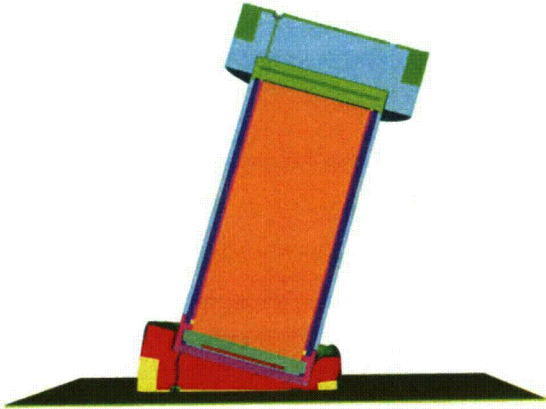


Figure III-34. Rail-Lead cask corner impact at 97 KPH (60 MPH)

Time = 0.03500

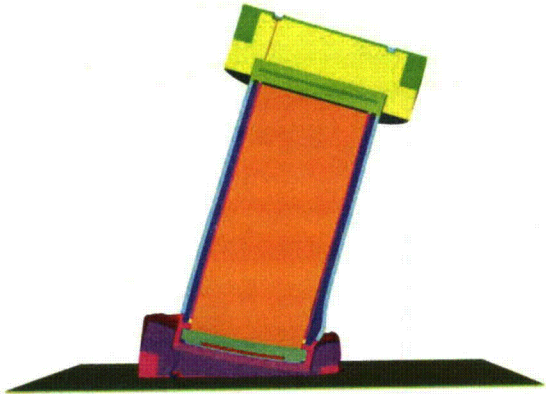


Figure III-35. Rail-Lead cask corner impact at 145 KPH (90 MPH)

Time = 0.03500

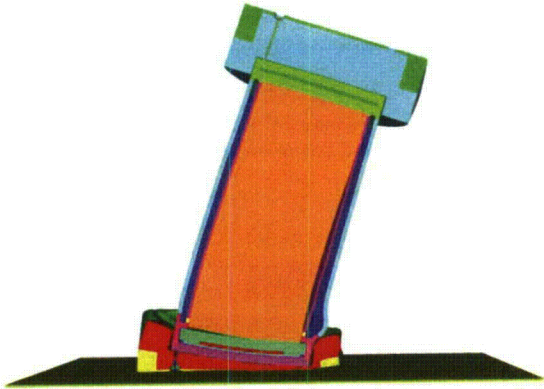


Figure III-36. Rail-Lead cask corner impact at 193 KPH (120 MPH)

Time = 0.03000

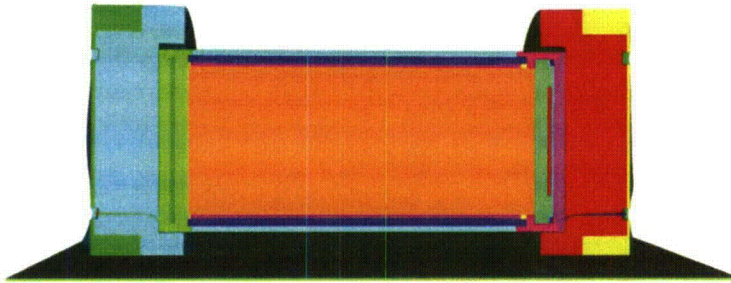


Figure III-37. Rail-Lead cask side impact at 48 KPH (30 MPH)

Time = 0.03000



Figure III-38. Rail-Lead cask side impact at 97 KPH (60 MPH)

Time = 0.02400



Figure III-39. Rail-Lead cask side impact at 145 KPH (90 MPH)

Time = 0.01800



Figure III-40. Rail-Lead cask side impact at 193 KPH (120 MPH)

III.2.6 Determination of Lid Gaps

Possible gaps between the lids and the cask were extracted from the final drop results. The longitudinal orientation of the cask was along the y-direction, so the difference in y-direction displacement between the lid and the cask gave a measure of the gap. A node on the cask was paired with the nearest node on the lid for this gap calculation. The nodes did not align exactly in the xz plane. Two gap values were calculated for the end drop orientation since the deformations were axisymmetric. For side down and cg over corner orientations, gap values were calculated at 5 equally spaced locations around the half-circumference of the cask, as shown in Figures III-41 to III-43.

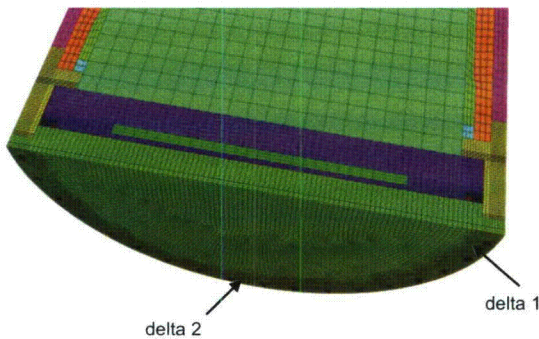


Figure III-41. Gap opening locations for end impact orientation

Comment [A13]: For section III.2.5 of the Appendix to stand alone, the results should be discussed here. At least a statement pointing to the discussion in Chapter 3, Sec 3.2.2, should be provided.

A note pointing to Table III-2, where "g" loads are given, would be useful to the general reader.

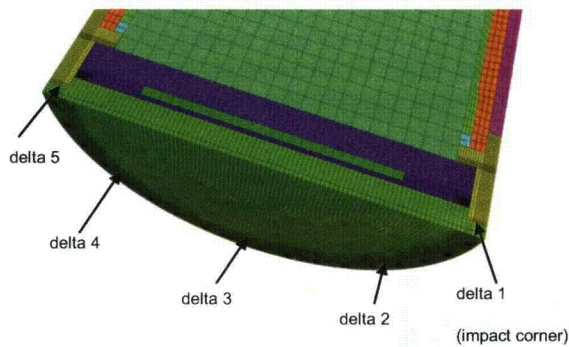


Figure III-42. Gap opening locations for corner impact orientation

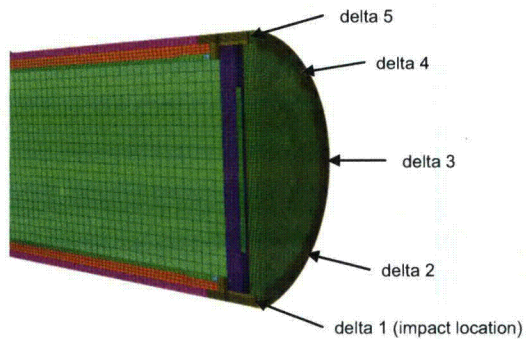


Figure III-43. Gap opening locations for side impact orientation

The next set of figures show plots of the gap sizes as a function of time for the inner and outer lid for each analysis case. All of the gaps calculated are somewhat conservative because the bolts did not include any pre-load. Pre-load decreased the gap size because the bolts do not start to elongate until the pre-load is overcome. As an example, if the 7.1-inch long inner lid bolts are pre-loaded to 50% of their yield strength ($0.5 \times 150.8 = 75.4$ ksi) the elastic elongation is 0.018 inches. This indicates the calculated gap for the inner lid is probably overestimated by this amount.

Comment [A14]: This discussion of preload is useful, if brief, and could be incorporated earlier. Some discussion of the effect of the presence of preload on response of other structural members would also be helpful.

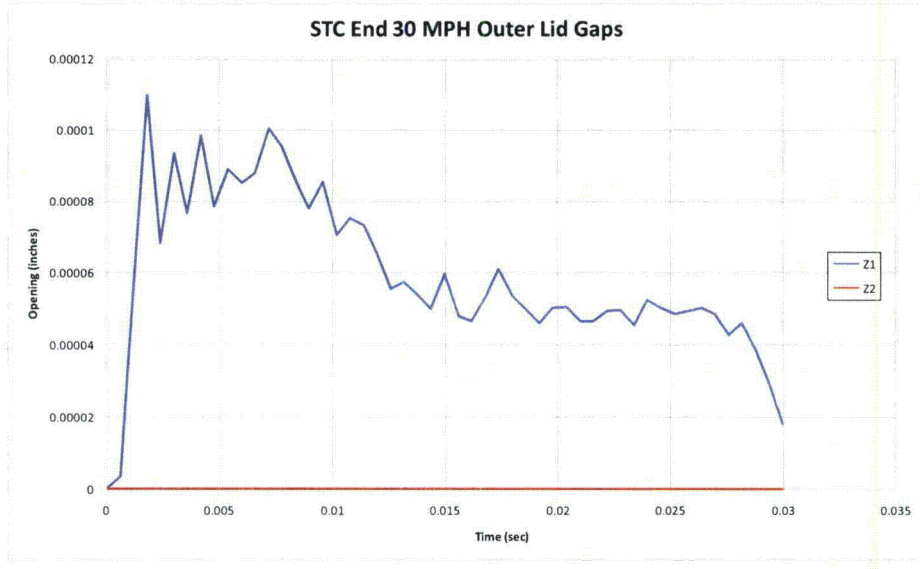
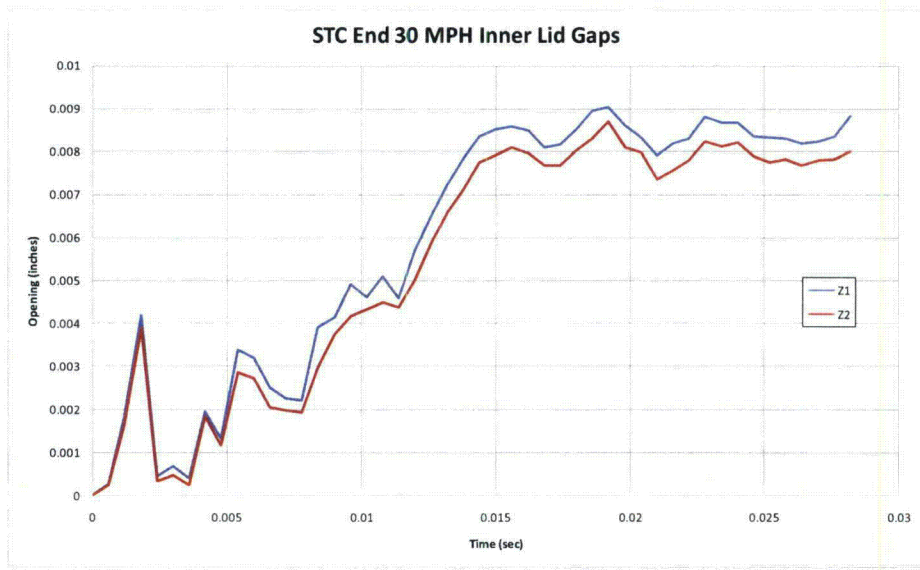


Figure III-44. Gaps in the inner and outer lids of the Rail-Lead cask from the end impact at 48 KPH (30 MPH)

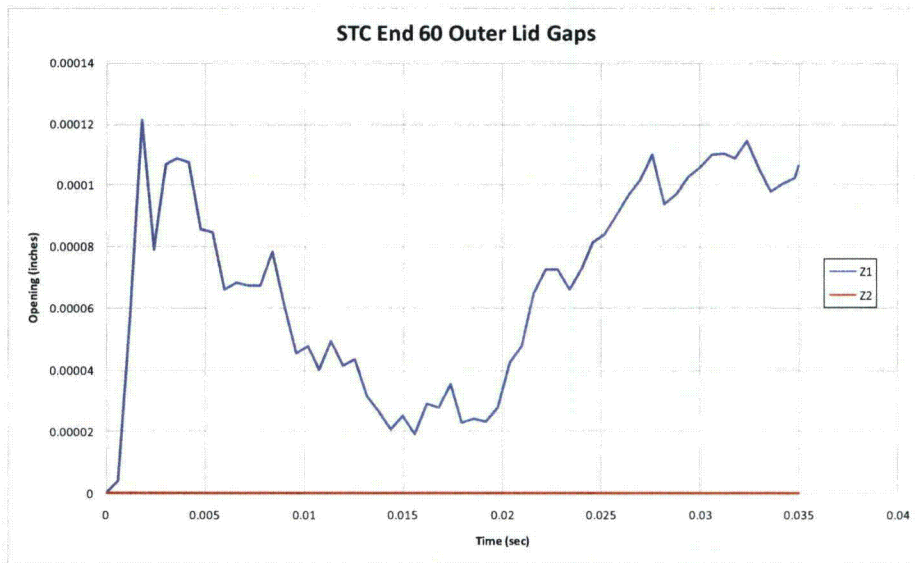
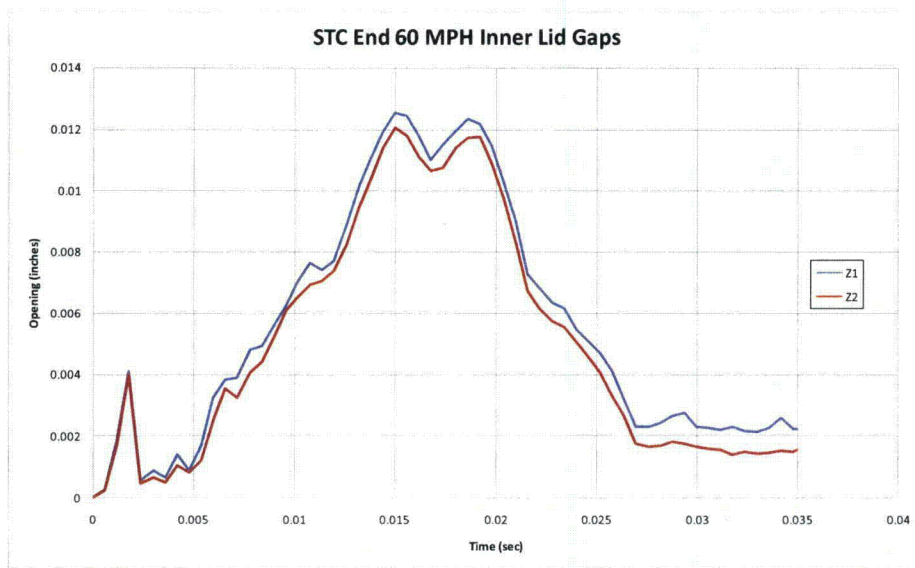


Figure III-45. Gaps in the inner and outer lids of the Rail-Lead cask from the end impact at 97 KPH (60 MPH)

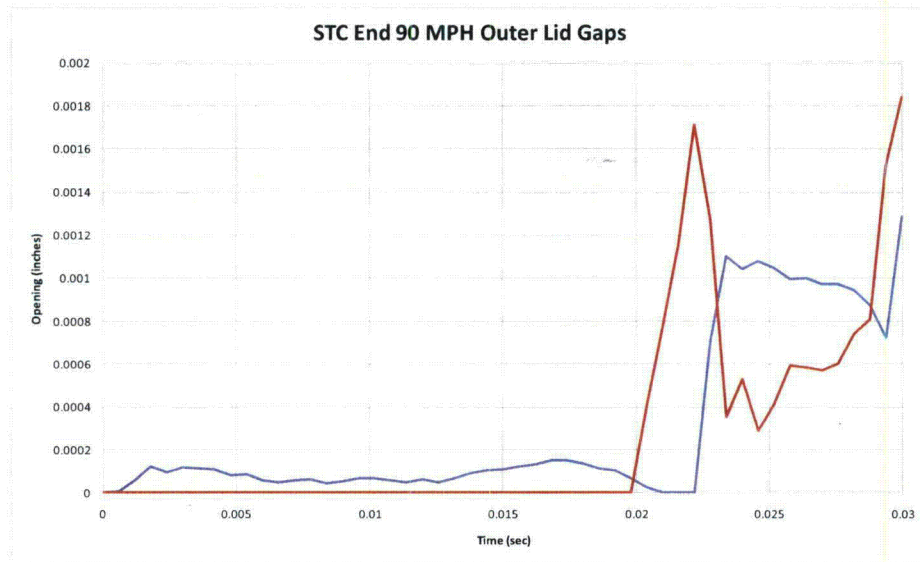
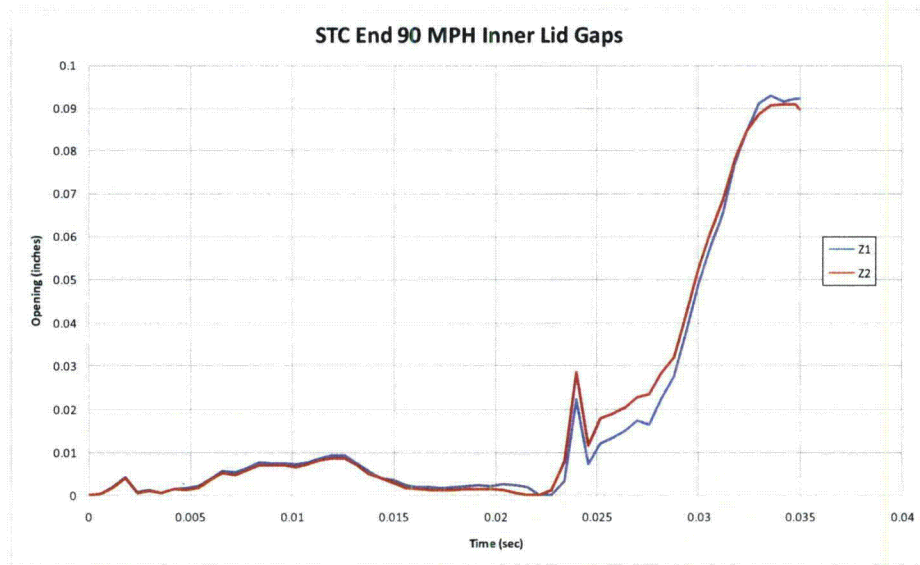


Figure III-46. Gaps in the inner and outer lids of the Rail-Lead cask from the end impact at 145 KPH (90 MPH)

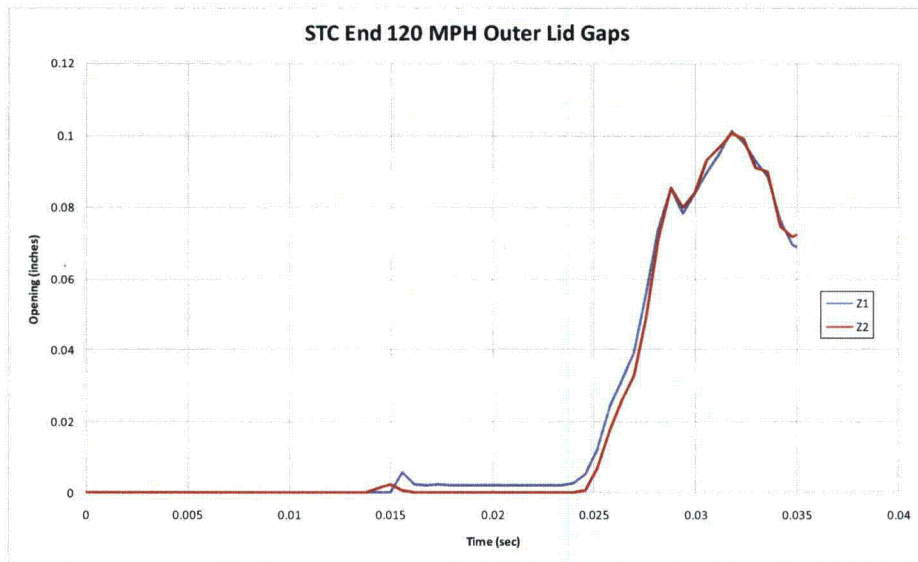
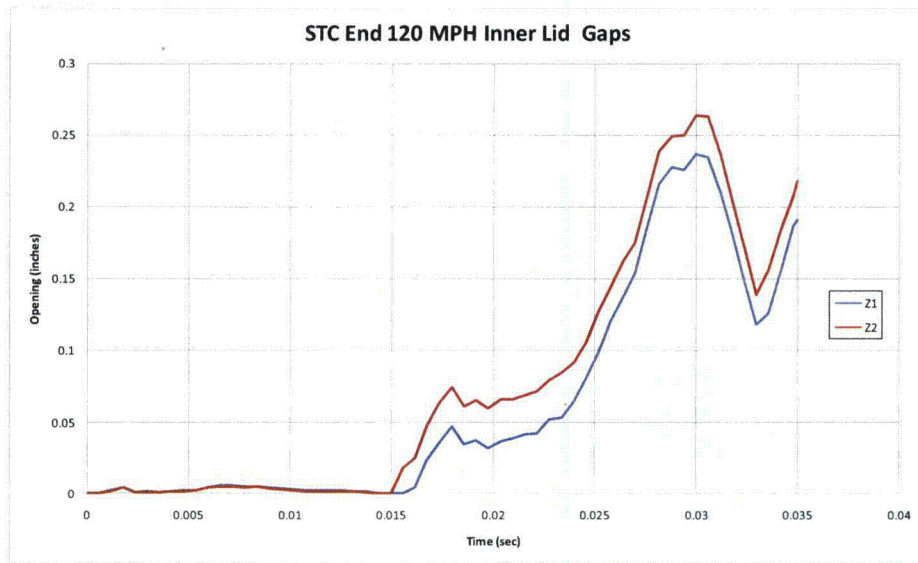


Figure III-47. Gaps in the inner and outer lids of the Rail-Lead cask from the end impact at 193 KPH (120 MPH)

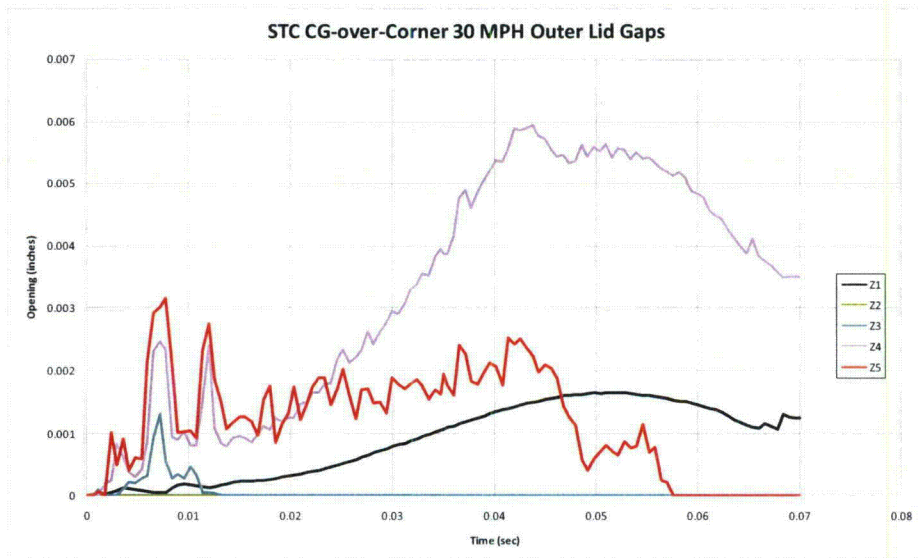
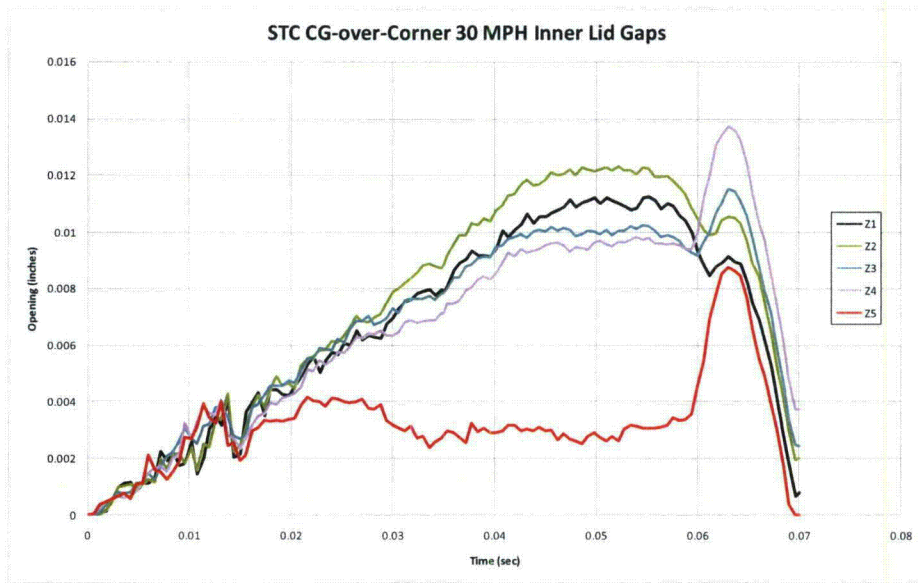


Figure III-48. Gaps in the inner and outer lids of the Rail-Lead cask from the corner impact at 48 KPH (30 MPH)

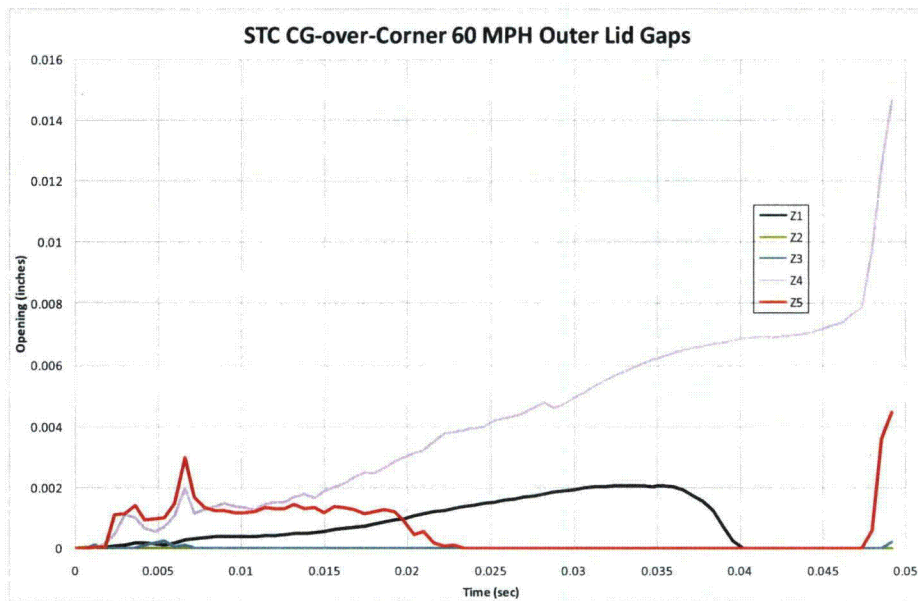
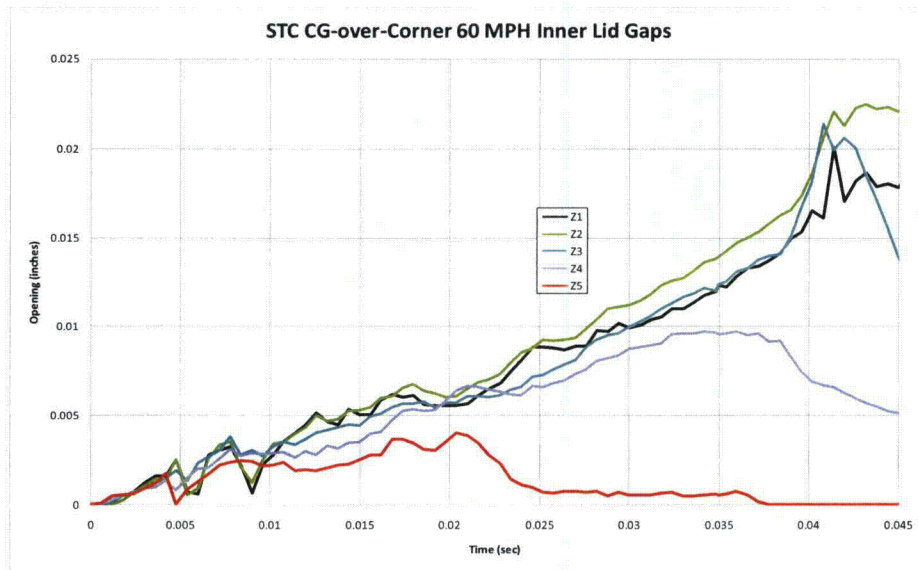


Figure III-49. Gaps in the inner and outer lids of the Rail-Lead cask from the corner impact at 97 KPH (60 MPH)

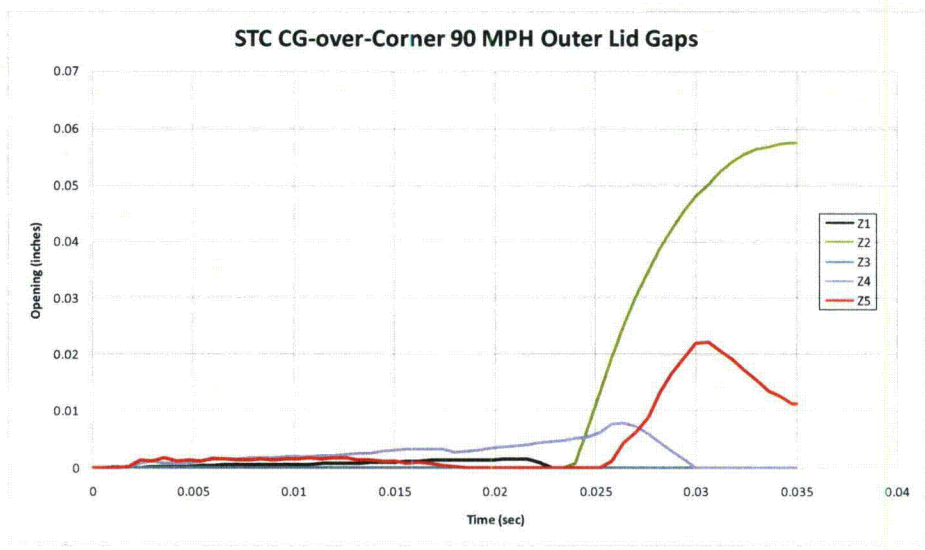
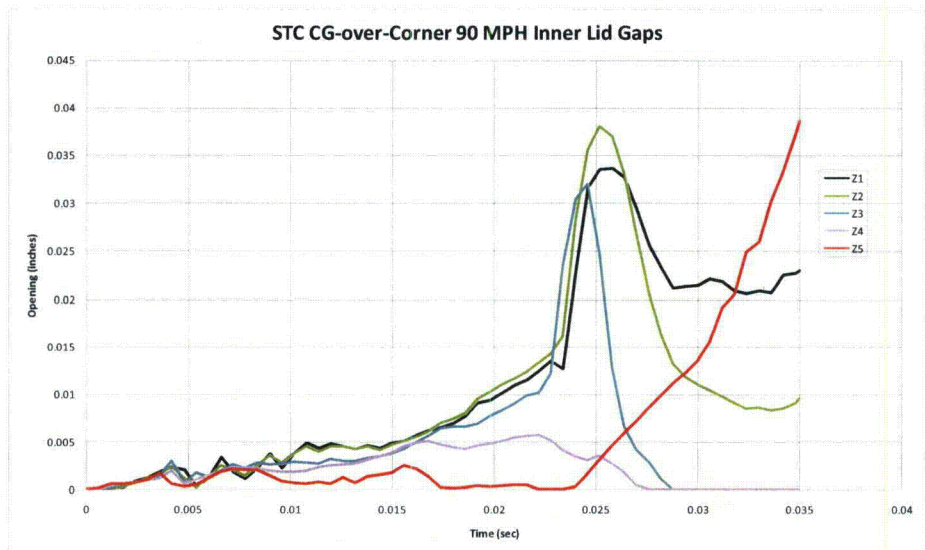


Figure III-50. Gaps in the inner and outer lids of the Rail-Lead cask from the corner impact at 145 KPH (90 MPH)

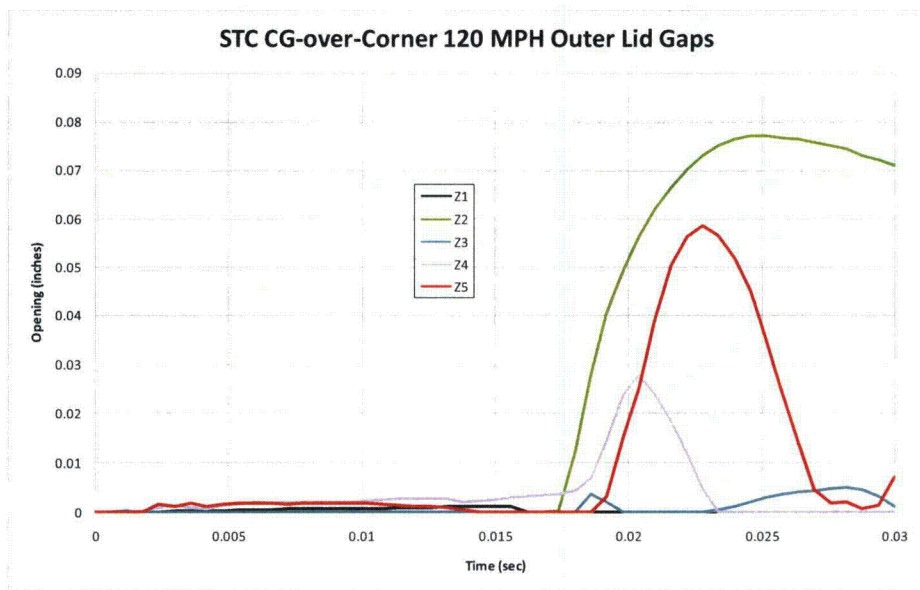
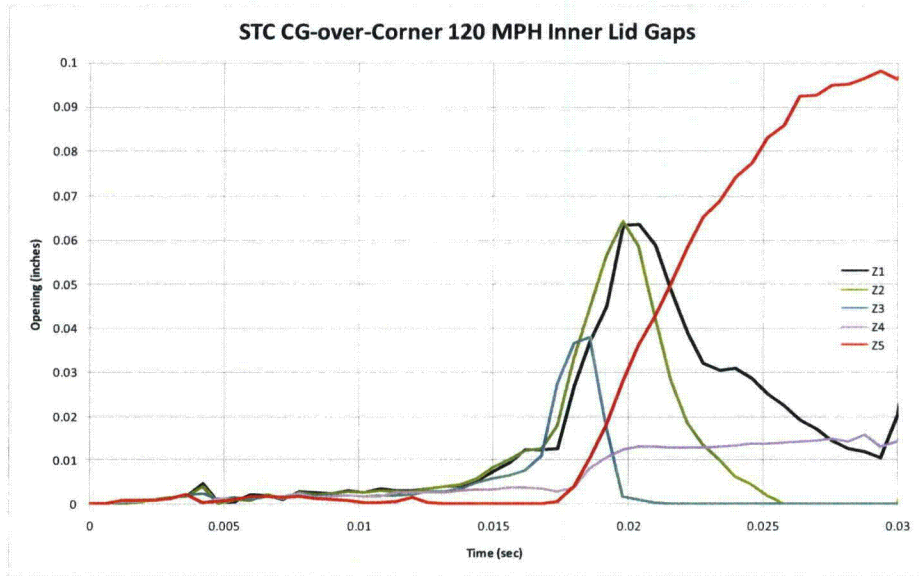


Figure III-51. Gaps in the inner and outer lids of the Rail-Lead cask from the corner impact at 193 KPH (120 MPH)

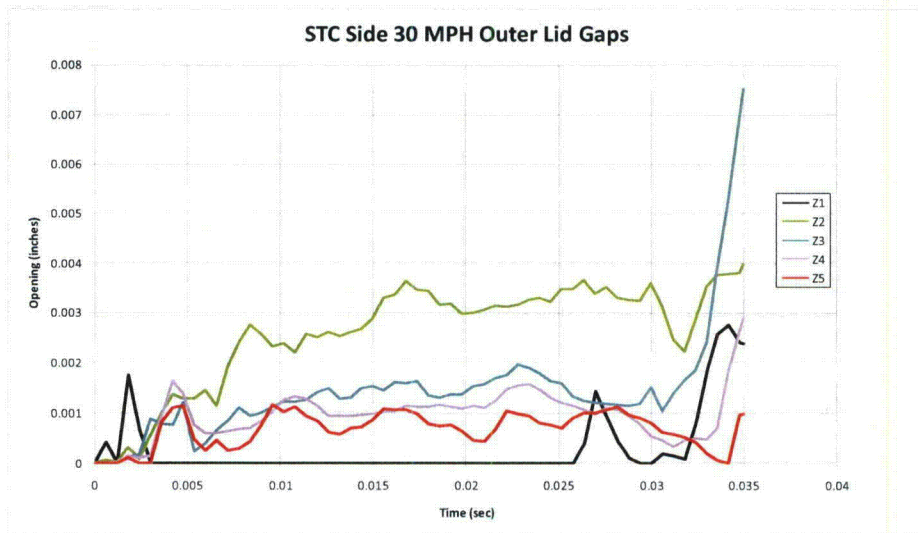
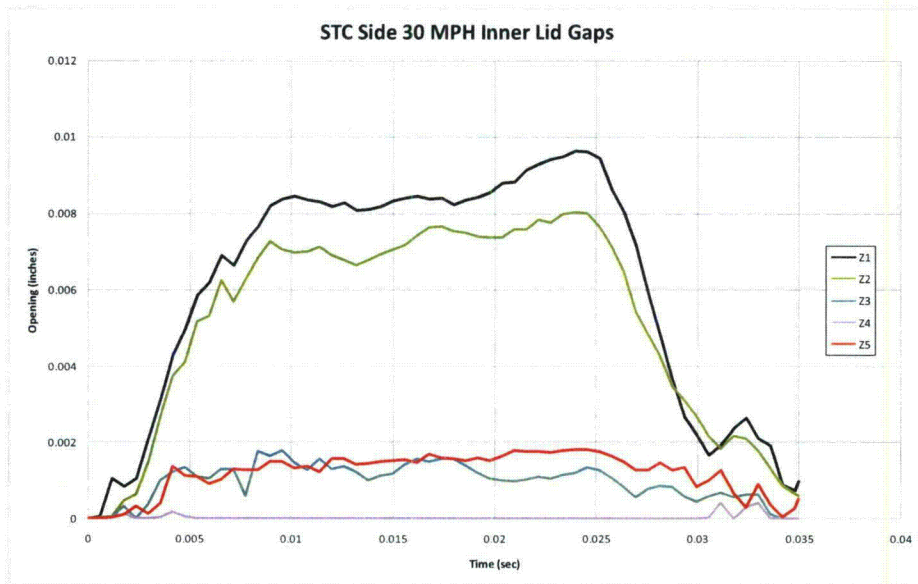


Figure III-52. Gaps in the inner and outer lids of the Rail-Lead cask from the side impact at 48 KPH (30 MPH)

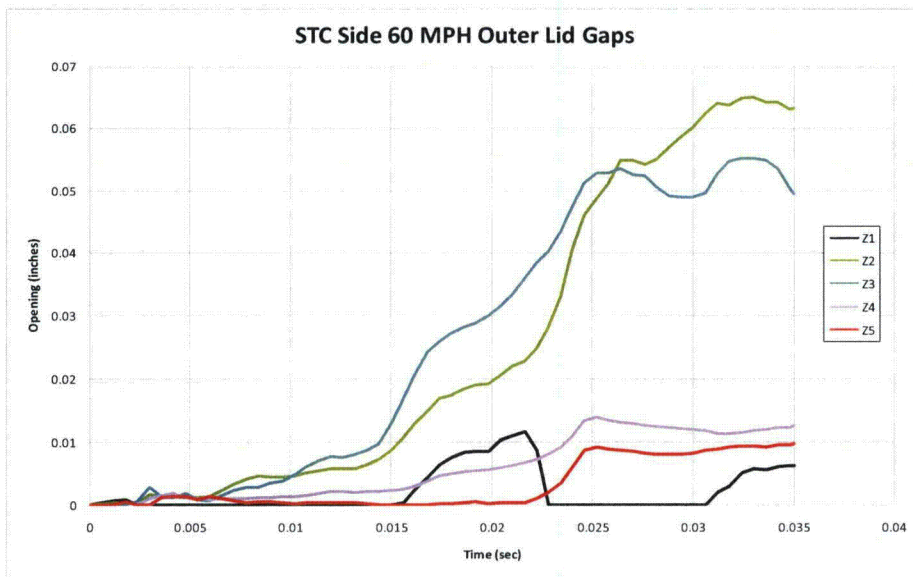
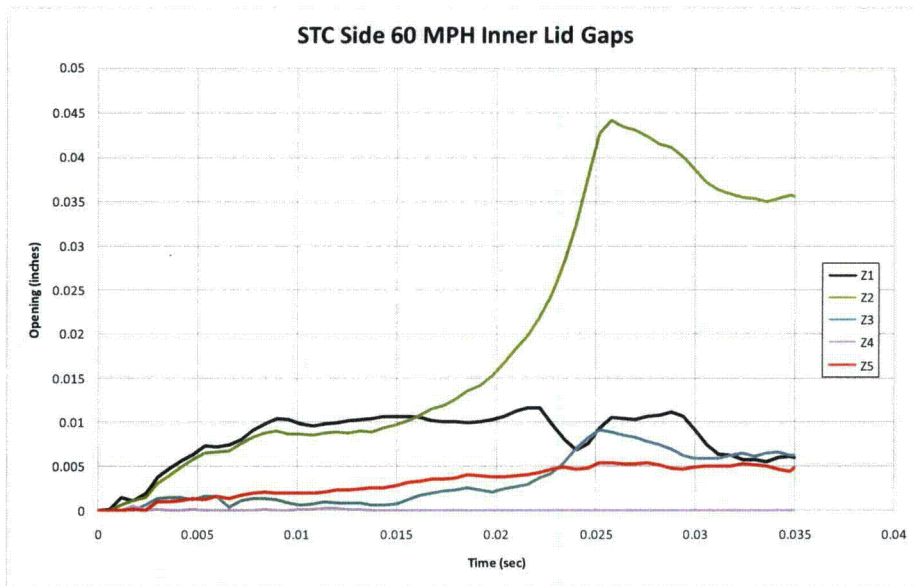


Figure III-53. Gaps in the inner and outer lids of the Rail-Lead cask from the side impact at 97 KPH (60 MPH)

To calculate any leak size based upon the gaps the compliance of the o-rings had to be taken into account. The Rail-Lead cask can be sealed with either elastomeric o-rings or metallic o-rings. Elastomeric o-rings can typically maintain a seal when the opening between the mating surfaces opens by 2.5 mm (0.10 in.), and this number is used as the compliance for the cases with elastomeric o-rings. Metallic o-rings are much less tolerant to gaps, and a value of 0.25 mm (0.010 in.) is used as the compliance for the cases with metallic o-rings. For the end impact analyses the gap size is uniform for the entire circumference of the seal, and the hole size is calculated by subtracting the compliance of the o-ring from the gap and multiplying by the circumference. If either the inner seal or the outer seal has a gap less than the compliance, then there is no leak area. For end impacts the only case where there is any leakage is for the 193 KPH (120 MPH) impact with metallic o-rings.

For the corner and side impacts the amount of gap varies around the circumference of the seal, and a more complicated algorithm is needed to calculate the hole size. As in the end impact, the compliance of the seal is subtracted from the gap and a trapezoidal area between measurement locations is assumed. In the corner impact, none of the gaps is large enough to overcome the compliance of elastomeric o-rings, but there would be some leakage for the 97, 145, and 193 KPH (60, 90, and 120 MPH) impacts. The calculated hole sizes for these three cases are 65, 599, and 1716 mm², respectively. In the side impact at 97 KPH (60 MPH) the gaps are not sufficient to cause a leakage with elastomeric seals, but with metallic seals a hole size of 799 mm² is calculated. In the 145 and 193 KPH (90 and 120 MPH) analyses there are a number of failed bolts and very large openings between the lids and the cask body. In these cases both the elastomeric and metallic seals fail and the resulting hole size is more than 10,000 mm². Table III-1 gives the final gap and hole sizes for each of the analyses.

Comment [A15]: As noted earlier, this value was reported for a particular case of an O-ring with a ¼ in. cross sectional diameter, compressed to 75%. This is an optimistic upper limit for the case studied. These limitations should be acknowledged here.

Table III-1. Available areas for leakage from the Rail-Lead cask

Orientation	Speed (KPH)	Location	Lid Gap (mm)	Seal Type	Hole Size (mm ²)
End	48	Inner	0.226	Metal	none
		Outer	0	Elastomer	none
	97	Inner	0.056	Metal	none
		Outer	0.003	Elastomer	none
	145	Inner	2.311	Metal	none
		Outer	0.047	Elastomer	none
	193	Inner	5.588	Metal	8796
		Outer	1.829	Elastomer	none
Corner	48	Inner	0.094	Metal	none
		Outer	0.089	Elastomer	none
	97	Inner	0.559	Metal	65
		Outer	0.381	Elastomer	none
	145	Inner	0.980	Metal	599
		Outer	1.448	Elastomer	none
	193	Inner	2.464	Metal	1716
		Outer	1.803	Elastomer	none
Side	48	Inner	0.245	Metal	none
		Outer	0.191	Elastomer	none
	97	Inner	0.914	Metal	799
		Outer	1.600	Elastomer	none
	145	Inner	8*	Metal	>10000
		Outer	25*	Elastomer	>10000
	193	Inner	15*	Metal	>10000
		Outer	50*	Elastomer	>10000

III.2.7 Acknowledgements

Jim Bean at Sandia contributed significantly to the development of this model.

III.3 Impacts onto Yielding Targets

III.3.1 Introduction

The finite element results discussed in the previous section are all for impacts onto a rigid target. For this type of impact, the entire kinetic energy of the impact is absorbed by the cask. For finite element analyses a rigid target is easily implemented by enforcing a no displacement boundary condition at the target surface. In real life, the construction of a rigid target is impossible, but it is possible to construct a target that is sufficiently rigid that increasing its rigidity does not increase the amount of damage to the cask. This is because in real impacts there is a sharing of energy absorption between the cask and the target. If the target is much weaker than the cask, the target will absorb most of the energy. If the target is much stronger than the cask, most of the energy will be absorbed by the cask. In this section the partitioning of the drop energy between the four generic casks and several "real-world" targets will be developed in order to obtain impact speeds

onto real surfaces that give the same damage as impacts onto rigid targets. Impacts onto hard desert soil, concrete highways, and hard rock are considered. Impacts onto water surfaces are not explicitly treated, but are discussed. In addition, the probability of puncture of the cask caused by impact against a non-flat surface (or impact by a puncture probe) is developed.

III.3.2 Method

For each finite element calculation for impact onto a rigid target the total kinetic energy of the finite element model is output at 100 time-steps through the analysis. The total kinetic energy is one half of the sum of the mass associated with each node times the velocity of that node squared. Figure III-54 shows kinetic energy time-histories for the steel-lead-steel truck cask for each orientation from the 120-mph impact analyses with pre-crushed impact limiters. From the time-history of kinetic energy, a velocity time history is derived. The rigid-body velocity for each time-step is calculated assuming that all of the kinetic energy of the model is caused by velocity in the direction of the impact. Equation III-1 shows this mathematically.

$$v_t = \sqrt{\frac{2KE_t}{\sum m_i}} \quad (\text{Eq. III-1})$$

where v_t is the velocity at time t , KE_t is the kinetic energy at time t , m_i is the mass associated with node i , and the summation is over all of the nodes in the finite element model.

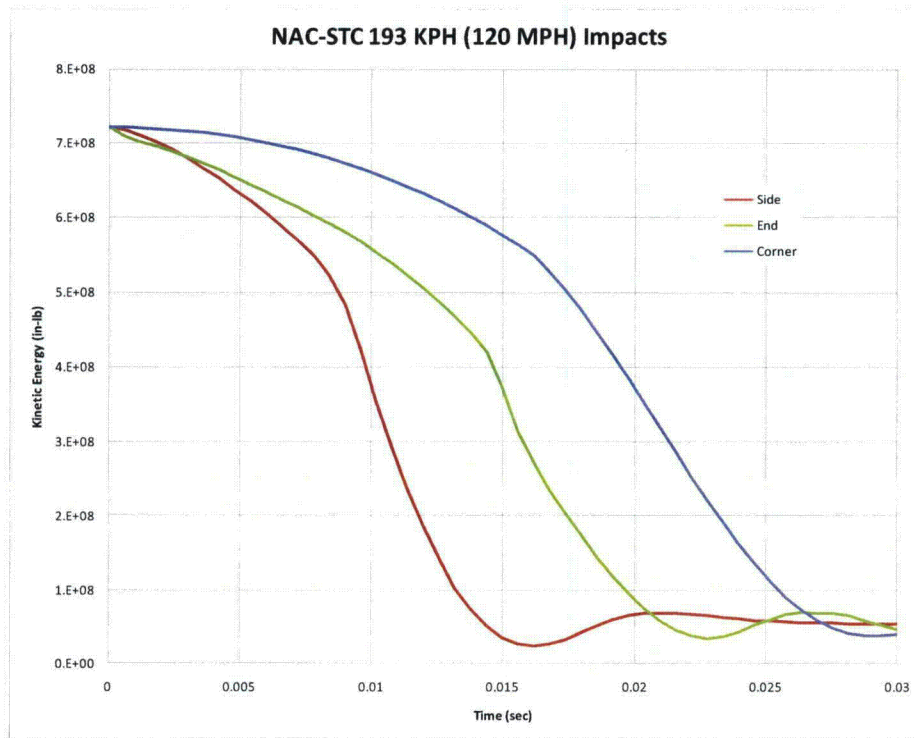


Figure III-54. Kinetic energy time histories for the Rail-Lead cask from 193 KPH (120 MPH) impact analyses in the end, side, and corner orientations

For each analysis the peak contact force is determined. Table III-2 lists these forces. For an impact onto a real target to be as damaging to the cask as the impact onto the rigid target, the target must be able to impart a force equal to this peak force to the cask.

The energy absorbed by the target in developing this force is added to the initial kinetic energy of the cask. This total absorbed energy is used to calculate an equivalent velocity by replacing KE_i in Equation III-1 with the total energy.

Comment [A16]: This is OK, but it should be noted that, since the loaded cask is a complex structure, there will not be an exact equivalence.

Comment [A17]: Agree with this basis.

Table III-2. Peak contact force for the Rail-Lead cask impacts onto an unyielding target (bold numbers are for the cases where there may be seal leaks)

Orientation	Speed (KPH)	Accel. (G)	Contact Force (Millions of Pounds)	Contact Force (MN)
End	48	58.5	14.6	65.0
	97	111.6	27.9	123.9
	145	357.6	89.3	397.1
	193	555.5	138.7	616.8
Corner	48	36.8	9.2	40.9
	97	132.2	33.0	146.8
	145	256.7	64.1	285.1
	193	375.7	93.8	417.2
Side	48	76.1	19.0	84.5
	97	178.1	44.5	197.8
	145	411.3	102.7	456.7
	193	601.1	150.0	667.4

III.3.3 Soil Targets

The force that hard desert soil imparts onto a cask following an impact was derived from results of impact tests performed by Gonzales [5-13], Waddoups [5-14], and Bonzon and Schamaun [5-15]. The tests by Gonzales and Waddoups used casks that were comparable to Rail-Lead cask, but much smaller. The tests by Bonzon and Schamaun were with casks that were less stiff than the Rail-Lead cask. This large amount of test data was used to develop an empirical soil target force-deflection equation that is a function of impactor area. Figure III-54 shows the force-deflection curves for impact of the Rail-Lead cask onto a soil target. Corner impacts were assumed to have the same contact area on the soil target as the end impacts, so only two curves are shown. Similar curves were developed for each of the other casks. Comparison of Figure III-55 with the forces in Table III-2 show that many of the impacts will result in very large soil penetrations. This is consistent with the results seen in Waddoups' tests, where casks were dropped 2,000 feet from a helicopter. Penetration depths for these impacts were up to 8 feet, and the equivalent rigid target impact velocity was less than 30 mph. Integration of the force-deflection curve up to the peak contact force determines the amount of energy absorbed by the target.

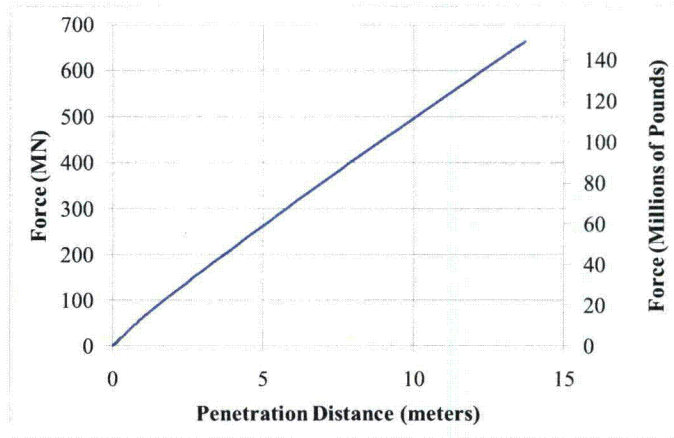


Figure III-55. Force generated by the Rail-Lead cask penetrating hard desert soil

III.3.4 Concrete Targets

The force imparted to a cask by impact onto a concrete target is derived from test results by Gonzales [5-13]. In his series of tests, a cask-like test unit impacted two types of concrete targets, one 12 inches thick and one 18 inches thick, at velocities from 30 to 60 mph. All of the impacts were in an end-on orientation. Based upon the results of these tests and engineering mechanics, an empirical relationship between the force and energy absorbed was derived. For impacts onto concrete slab targets there are two mechanisms that produce large forces onto the cask. The first is the generation of a shear plug in the concrete. The force required to produce this shear plug is linearly related to the impact velocity, the diameter of the impacting body, and the thickness of the concrete. Equation III-2 gives the empirical equation for the force required to produce the shear plug.

$$F_s = C_s v_e d_i t_c \quad (\text{Eq. III-2})$$

where F_s is the force required to produce the shear plug, C_s is an empirical constant (16.84), v_e is the equivalent impact velocity, d_i is the diameter of the impactor, and t_c is the thickness of the concrete slab.

The energy absorbed in producing this shear plug is linearly related to the cask diameter, the square of the impact velocity, and the fourth root of the slab thickness. Equation III-3 gives the empirical equation for the energy required to produce the shear plug.

Comment [A18]: Or "struck"

Deleted: was

Formatted: Font: (Default) Times, 12 pt, Highlight

Formatted: Highlight

Formatted: Font: (Default) Times, 12 pt, Highlight

Deleted: onto

$$E_s = C_e d_1 v_c^2 t_c^{0.25} \quad (\text{Eq. III-3})$$

where E_s is the energy required to produce the shear plug and C_e is an empirical constant (0.00676).

After the shear plug is formed, further resistance to penetration is achieved by the behavior of the subgrade and soil beneath the concrete. This material is being penetrated by the cask and the shear plug. Generally, the shear plug forms with 45-degree slopes on the side. Therefore, the diameter of the soil being penetrated is equal to the cask diameter plus twice the slab thickness. The behavior of the subgrade and soil is assumed to be the same as the hard desert soil used for the soil target impacts. Figure III-56 shows a comparison of the empirical relationship with one of Gonzales' tests. For corner and side impacts an equivalent diameter is calculated to fit with the empirical equations. For each case the diameter is calculated by assuming the shear plug forms when the concrete target has been penetrated two inches. The area of the equivalent diameter is equal to the area of the concrete in contact with the cask when the penetration depth is two inches. To calculate the equivalent velocity for concrete targets the force required to generate the shear plug must be compared to the peak contact force for the impact onto the rigid target. The velocity required to produce this force can be calculated from Equation III-2. The kinetic energy associated with this velocity is absorbed by a combination of producing the shear plug, penetration of the subgrade and soil beneath the concrete, and deformation of the cask. The energy absorbed in producing the shear plug is calculated by Equation III-3, the energy absorbed by the cask is equal to the kinetic energy of the rigid target impact, and the energy absorbed by the subgrade and soil is calculated in a manner similar to that for the soil impact discussed above. If the amount of energy to be absorbed by the soil is sufficiently high, the force in the soil will be higher than the force required to produce the shear plug. In this case, an iterative approach is necessary to derive an equivalent velocity so that the maximum force generated in penetrating the subgrade and soil beneath the concrete is equal to the peak contact force for the rigid target impact.

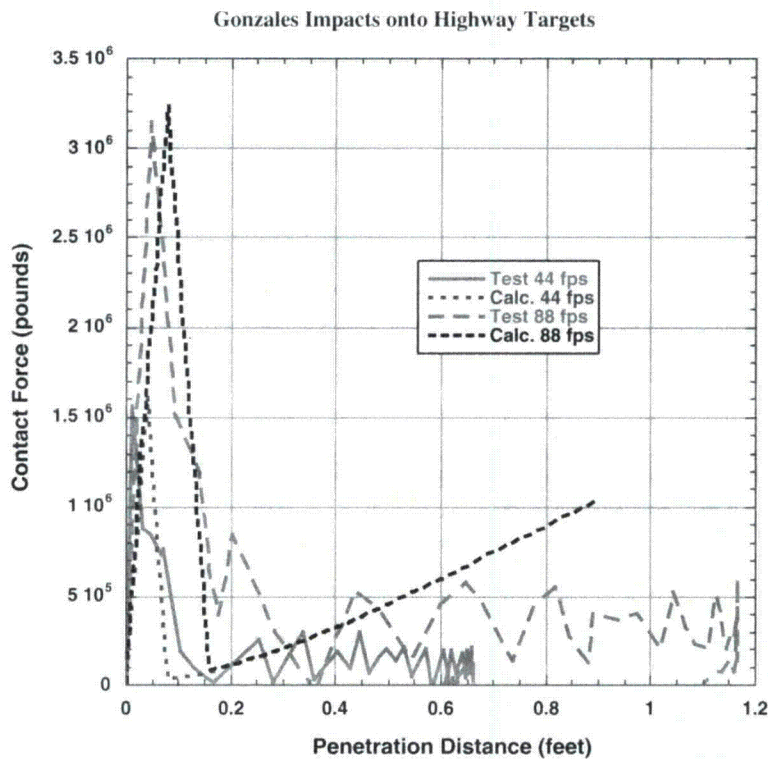


Figure III-56. Comparison of test force-deflection curves with those derived from the empirical equations.

The only orientation of impacts onto concrete targets where test data is available is for end impacts. In this orientation the contact area between the cask and the concrete does not increase with increasing penetration distance. In order to use the empirical relationships developed for end impacts with other impact orientations, an equivalent diameter must be determined. For both the side and corner impacts, the equivalent diameter was calculated to have an area equal to the area of the cask two inches above the contact point. For side impact orientations, this area is a rectangle. For corner impact orientations this area is a truncated parabola.

III.3.5 Hard Rock Targets

For impacts onto hard rock targets the target is assumed to be a semi-infinite half plane. The force and energy absorbed by the target is determined by the volumetric behavior of the rock. For hard rock surfaces this behavior is sufficiently stiff that very little energy is absorbed by the target. For this reason these impacts are treated as rigid target impacts.

Comment [A19]: Is there a basis for this? For example, does this correspond to the flattened side dimension of a cask dropped in a horizontal orientation at the given velocity?

III.3.6 Results for Real Target Calculations

Table III-3 gives the results for impacts onto soil and concrete targets.

Table III-3. Equivalent velocities for Rail-Lead cask impacts onto various targets, KPH

Orientation	Rigid	Soil	Concrete
End	48	102	71
	97	205	136
	145	>250	>250
	193	>250	>250
Corner	48	73	70
	97	236	161
	145	>250	>250
	193	>250	>250
Side	48	103	79
	97	246	185
	145	>250	>250
	193	>250	>250

III.3.7 Impacts onto Water

Equivalent velocities for impacts onto water targets for velocities greater than the regulatory impact are assumed to be above the range of possible impact velocities (150 mph). The incompressible nature of water makes perfectly flat impacts quite severe. As the impact velocity increases smaller deviations from the perfectly flat orientation are sufficient to cause the lack of shear strength in water to dominate the response. Because perfectly flat impacts are very improbable, this approach is justified.

III.4 Response of Spent Fuel Assemblies

III.4.1 Introduction

The response of spent power reactor fuel assemblies to impact accidents is not well understood. While this area has been investigated in the past (Sanders et al. 1992), those models tended to be relatively crude and imprecise. In addition, there is a renewed interest on the part of utility companies in shipping higher burnup spent fuel. Therefore, determining a more accurate response of spent fuel assembly to impact loads that may be the result of transportation or handling accidents or malevolent acts is essential. Sandia National Laboratories has performed a series of computational analyses to predict the structural response of a spent nuclear fuel assembly that is subjected to a hypothetical regulatory impact accident, as defined in 10 CFR71.73. This study performs a structural analysis of a typical pressurized water reactor (PWR) fuel assembly using the Abaqus/Explicit finite element analysis code. The configuration of the pellet/cladding interface and the material properties of the pellet have been varied in the model to account for possible variations in actual spent fuel assemblies.

Comment [A20]: In some of the recent literature, the term "used" is appearing, in place of "spent". Is there any benefit in recognizing this alternate usage in this NUREG?

III.4.2 Description and Method

A typical PWR fuel assembly is shown in Figure III-57. The assembly consists of a series of fuel pins, or rods, grouped together in a square array. The fuel rods are held in place by a series of equally spaced grids. Within the array of fuel tubes are a series of guide tubes in which control rods are placed for controlling the fission reaction during operation. The guide tubes are attached to endplates, nozzles or end fittings, which provide rigidity for handling.

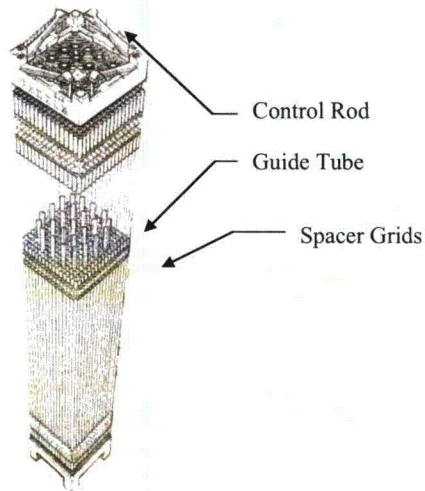


Figure III-57. PWR fuel assembly

An individual fuel rod is shown schematically in Figure . It is constructed by stacking a series of Uranium Dioxide (UO_2) pellets inside a Zirconium tube, placing a spring on the top of the pellet stack and welding on end caps. A plenum is added at the top of the assembly to provide a sufficient volume to collect released fission gases.

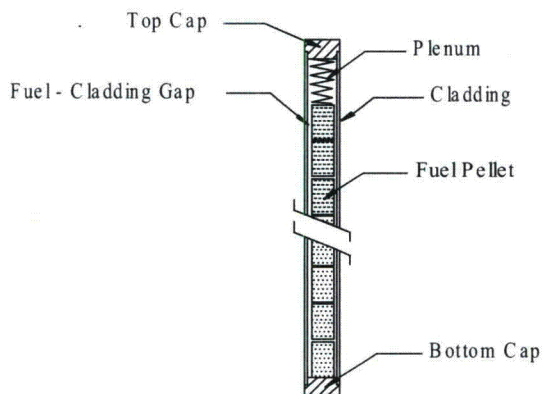


Figure III-58. Fuel rod schematic drawing

The working environment of a reactor is extremely harsh. The fuel rods are subjected to neutron radiation, large thermal gradients, large stress due to external water pressure and large local stress from contact between the pellet and the cladding. Upon the first power cycle, the uranium pellet cracks into pie shaped pieces due to the large radial temperature gradients across the pellet. Over a short period of time (months), the pellets shrink as fine porosity in the fuel is removed by radiation densifications. The cladding slowly creeps down onto the pellet due to its high operating temperature and the external pressure of the coolant. The pellet also begins to expand due to fission product swelling. Over a period of 1-2 years the initial gap between the fuel rod and the pellet is eliminated. However, the contact between the cladding and the fuel pellet is not necessarily circular and uniform. This leads to local increases in the cladding stress. In addition, zirconium is one of the few elements that react with both oxygen and hydrogen. This can lead to a reaction between the ZrO_2 layers on the inner cladding surface and the fuel pellet to form a bonding interface of $(U,Zr)O_2$ between the fuel pellet and the cladding. In essence, bonding the pellet to the cladding wall. In addition, hydride precipitants can also form in the Zircaloy cladding wall.

Upon the removal from the reactor, the state of the spent fuel assembly at any future time depends on the spent fuel's environmental history as well as its condition upon removal from the reactor. The internal gas pressure in a fuel rod having been removed from the reactor now provides tensile hoop and axial stresses on the cladding. This stress along with changes in cladding temperature may allow hydrogen to precipitate out and possibly reform along the circumferential directions (direction of highest stress). Plastic creep in the cladding may cause a gap to develop between the cladding and the fuel pellet and the development of void spaces in the cracked pellets. The current material conditions and stress state of any particular rod at the time of an accident is complex and unknown. Therefore, the current material properties and

Comment [A21]: Should this be "cracked"?

Formatted: Font: 12 pt, Highlight

Formatted: Highlight

Formatted: Font: 12 pt, Highlight

geometric configuration will be varied over a small range to attempt to account for the actual unknown material and geometric variations.

Table III-4 lists the material properties and nominal dimensions of a 17x17 PWR fuel assembly. Due to the large number of rods and the large ratio between the fuel assembly length and the fuel rod diameter, modeling a complete assembly using the finite element method is challenging. To build the entire model using continuum and structural shell elements with a high enough resolution in each fuel rod would produce a model with so many degrees of freedom as to be computationally intractable. Therefore, the current analysis will be broken down into three steps. In the first step, the entire assembly will be modeled using structural beam and shell elements. Then in the second step, the loads from the highest loaded rod in the full assembly model will be transferred to a single rod model constructed of continuum and structural shell elements. This model will provide the detailed stress field necessary to determine the integrity of the fuel rod. Due to the severe nature of the reactor environments there are significant material and geometric changes in the fuel rods. Very little if any test data is available for the Zircaloy-4 material under high irradiation conditions, therefore as a third step, a series of parametric analyses were conducted with the continuum model to determine the sensitivity of the model to changes in the rod geometry and the pellet and cladding material properties.

Table III-4. Properties of fuel assembly

Assembly Type 17 x 17	
Cladding Material	Zircaloy-4
Assembly Cross-section (in)	8.43-8.54
Number of Fuel Rods per Assembly	264
Fuel Rod OD (in)	0.374 to 0.379
Minimum Cladding Thickness	0.023
Pellet Diameter (in)	0.3225 to 0.3232
Maximum Active Fuel Length (in)	144

Comment [A22]: Suggest SI dimensions be provided, also.

III.4.3 Finite Element Models

As described above, two major models have been developed in this analysis. The first of these is the beam fuel assembly model which is a structural model consisting of beam and shell elements. This model is used to determine the overall response of the fuel assembly. Using data from this

Formatted: Font: 12 pt, Highlight

Deleted: T

model a detailed continuum model of a single rod is developed to determine a more detailed response of the most highly loaded rod. Several parametric analyses are conducted with the latter model to determine the effect of variations of rod material properties and geometry. In addition to these models, several smaller models have been developed to aid in the overall analysis. Initial models were developed to test the capabilities of the finite element codes. Small models were also developed when problems arose in the analyses. All of these models along with the final rod analysis are discussed in the following section.

Fuel Assembly Finite Element Model

Using the latest version of the Abaqus/Explicit finite element code, a complete fuel assembly model (shown in Figure III-59) was constructed and analyzed. It incorporates 3D beam elements for the fuel pins and control rods, and shell elements for the spacer grid assemblies and the support plates representing the basket walls. The endplates are modeled as solid plates using hexahedron elements so that the support rod beam elements can be attached. The model contains 265 fuel pins and 24 tie rods. There are a total of 129,440 elements, with 41,616 beam elements. There are 144 beam elements along the length of each fuel rod and support rod. The location of the guide tubes in the cross-section of the fuel assembly is presented in Figure III-60.

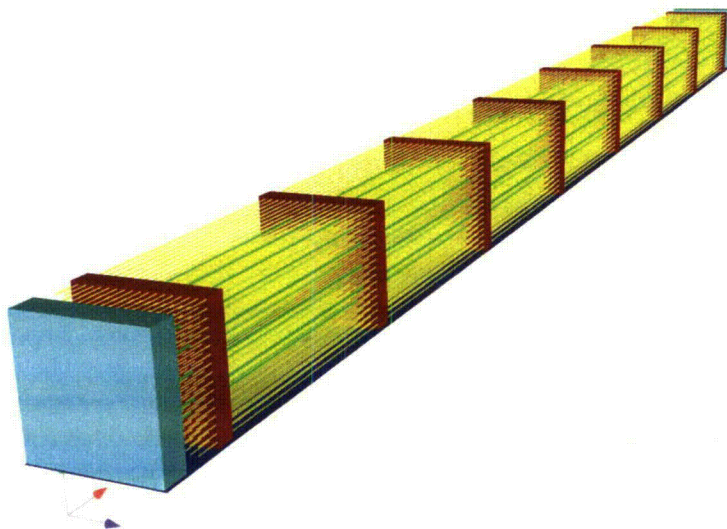


Figure III-59. Beam Fuel Assembly finite element model

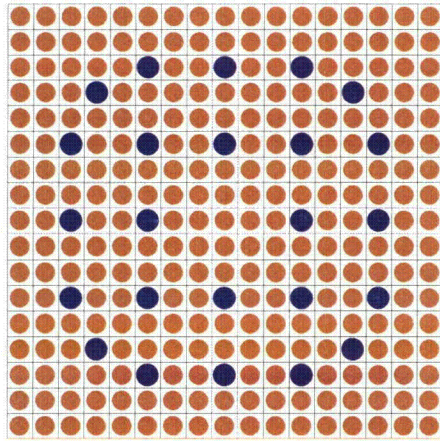


Figure III-60. Cross-section of 17x17 fuel assembly with guide tubes (in blue)

The fuel assembly model was loaded using acceleration curves developed from experimental data of a side impact drop test. The full-scale data for the analysis was calculated from the 1/4 scale test data. A plot of the full-scale data is presented in Figure III-61. An additional curve was generated from the full-scale data to yield a maximum acceleration of 100 g's, while maintaining the same total impulse. The fuel rods are given an initial velocity of 528 in/sec, which corresponds to a 9-meter drop test. The acceleration is applied to the lower plate, which represents the side of the fuel basket.

Comment [A23]: An explanation of the reason for not addressing the axial drop case would be helpful.

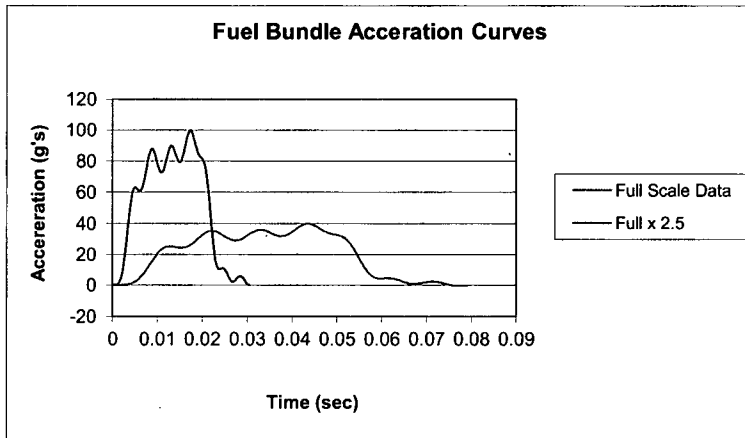


Figure III-61. Acceleration curves applied to fuel assembly beam model

The fuel rod material is modeled as unirradiated Zircaloy-4, using a power law hardening constitutive model fit to test data from the literature, Pierron et al. [5] The calculated material parameters are shown in Table III-5. These material properties are used for the fuel pins, the ties rods, and the support grid. In this analysis, the fuel pins and tie rods are modeled as solid beams with a circular cross-section.

Table III-5. Zircaloy-4 material parameters

Elastic Modulus	13.0 E3 ksi
Yield Stress	65 ksi
Luder Strain	0.00
Hardening Constant	103.5 ksi
Hardening Exponent	0.845

Fuel Assembly Model Results

For the lower acceleration curve given in Figure III-61, which represents a rail cask, there is no plastic deformation in the fuel rods or the spacer grids. The entire model remains elastic. For the analysis with the higher acceleration curve, there is no plastic deformation in the fuel rods and some plastic deformation in the spacer grids. Figure III-62 shows the most highly strained spacer grid. The lower three sections of the spacer grid buckle and a maximum plastic strain of 28% is calculated.

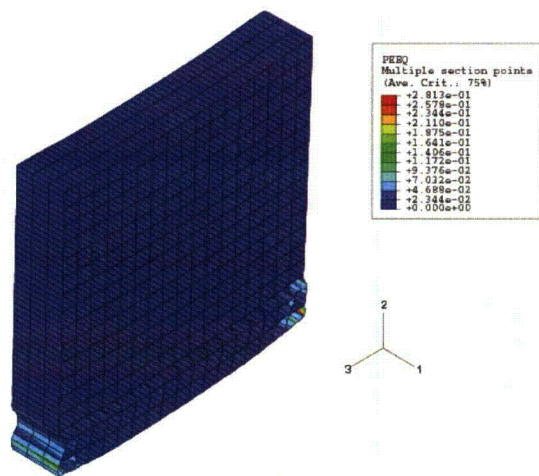


Figure III-62. Spacer grid 100g analysis plastic strain

The contact forces from the beam fuel assembly model will be used as input to a single rod continuum model. Since these forces occur over very short durations during the analysis, it was necessary to obtain data points at each time step in the fuel assembly model. Therefore, contact forces at a total of 20,349 time steps were obtained from the fuel assembly analysis.

Beam Element Versus Solid Element Contact

In processing the contact forces from the beam fuel assembly model, it was observed that the forces calculated during beam-to-beam contact were very large and acted over very short durations. They were much larger than the forces calculated in the model for the beam-to-shell contact. To investigate this difference in the magnitude and duration of the contact forces, two additional models were developed. The first, shown in Figure III-63, is a model of two impacting rods modeled with hexahedron elements. The second, shown in Figure III-64, is a model of two impacting rods modeled using beam elements. Since the beam elements in the beam fuel assembly model remain elastic, these models were evaluated for impact using elastic material properties.

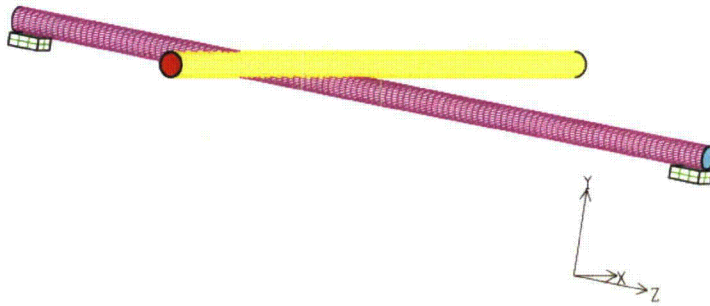


Figure III-63. Hexahedron test model for solid rod-to-rod contact in Abaqus/Explicit

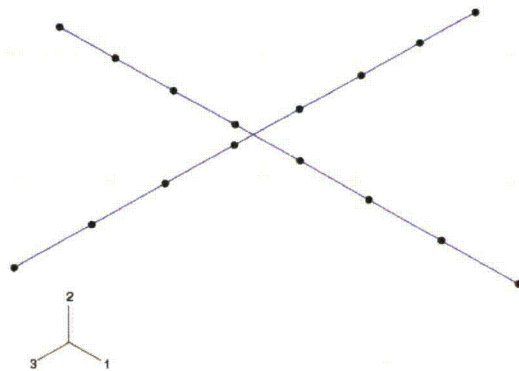


Figure III-64. Test model for beam-to-beam contact in Abaqus/Explicit

The results from the two finite element rod models are shown in Figure III-65 and Figure III-66. For the same mass, impact velocity and cross-sectional geometry, the two models generate two different sets of contact forces. As shown in Figure III-65, the beam element impact forces are much larger and shorter in duration than those generated from the hex rod model. The magnitudes of the forces differ by about a factor of five. An additional check was made comparing the hexahedron Abaqus/Explicit model to a similar model run in the Sandia code PRONTO3D. Both codes generated similar contact and reaction forces. Continued evaluation of the two models generated the curves shown in Figure III-66. For the velocity range of interest there is a good linear fit for each curve. Therefore, in transferring the loads between the beam fuel assembly model and the continuum beam model the magnitude of the forces were scaled in accordance with the curves in Figure 66. The length of each beam element impulse was increased to keep the integral of the curve the same. That is, the total impulse was maintained to conserve the change in momentum.

Comment [A24]: It appears that the analysis of the crossed rods is certainly conservative, with respect to contact stress, compared to the actual case where the rods are constrained to be essentially parallel. This should be noted in the discussion.

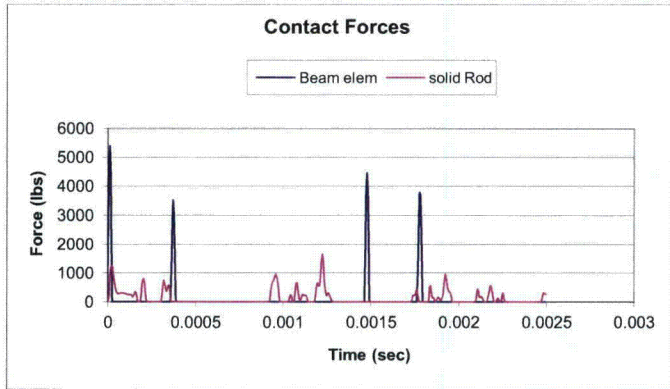


Figure III-65. Comparison of contact forces between solid rod and beam element rod

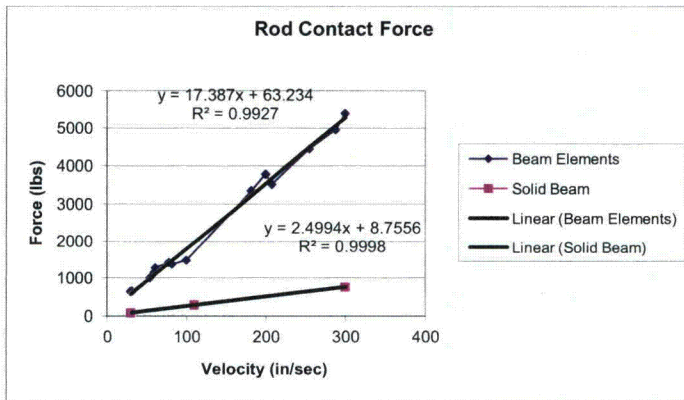


Figure III-66. Comparison of contact forces as a function of impact velocity

Continuum Rod Model

A continuum model was constructed using shell and hexahedral elements. The mesh is shown in Figure , with a blowup of the end region showing the mesh density. The magenta colored regions represent the locations of the spacer grids. There is a plane of symmetry along the longitudinal axis of the beam. The symmetric model contains 162,000 elements, with 139,000 hexahedron

elements used to model the UO_2 core and 23,000 shell elements used to model the Zircaloy-4 cladding. The hexahedron core has 16 elements across the diameter and there are 16 shell elements around the semicircular arc of the cladding.

The contact forces obtained from the beam fuel assembly model for the 100g loading are applied to a set of shell nodes running along the top and bottom of the symmetry plane. There are 1,446 nodes along each surface. Positive contact forces are applied to the bottom set of nodes and negative forces are applied to the upper nodes. As noted in the previous section the forces from the beam fuel assembly model that result from beam-to-beam contact are scaled according to the curves in Figure III-66 and the duration of the load is then increased to conserve the change in momentum. In the region of the spacer grid where there is beam-to-shell contact, the loads are not scaled. The new load curves are then interpolated from the element nodes in the beam fuel assembly model to a larger number of element nodes in the continuum model. The rod model is given the same initial velocity as the beam fuel assembly model, 528 in/sec.

Formatted: Font: 12 pt, Highlight

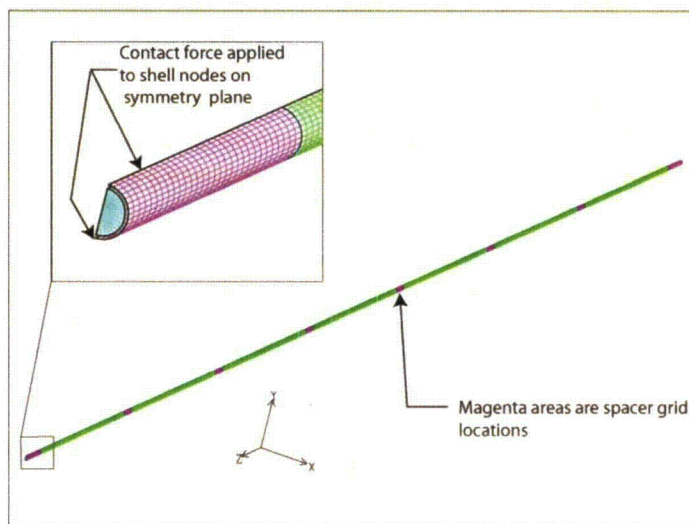


Figure III-67. Continuum rod finite element model

The rod materials are also modeled using a power-law hardening model. The parameters are presented in Table III-6. The model was run for two different load cases as shown in Table III-7. In the first case, the outside diameter of the UO_2 core and the inside diameter of the cladding are the same, the Zircaloy-4 material is modeled as unirradiated fuel and the UO_2 is also assumed to be pristine. In the second load case, the cladding material is assumed unirradiated, while the

modulus of the UO₂ is decreased by an order of magnitude to simulate a softer, crumbled material, which has been irradiated. The results from both of these analyses are presented in the following section.

Table III-6. Standard Material Properties

	Zircaloy	Uranium Oxide
Elastic Modulus	13.0 E3 ksi	28.0 E3 ksi
Yield Stress	65 ksi	21.6 ksi
Luder Strain	0.00	0.00
Hardening Constant	103.5 ksi	103.5 ksi
Hardening Exponent	0.845	0.845

Table III-7. Load case parameter changes

Load Case parameters			
Case	Cladding Yield Strength (psi)	UO ₂ Modulus (psi)	Cladding Gap (inches)
Case 1	65,250	28 x 10 ⁶	None
Case 2	65,250	28 x 10 ⁵	None

Continuum Rod Results

Analysis Case 1

The first analysis case models unirradiated Zircaloy-4 material with no gap between the UO₂ rod and the cladding. The resulting kinetic energy plot for this analysis case is presented in Figure III-68. Almost all of the kinetic energy is lost from the rod; this indicates that the load impulse applied in the continuum model matches the impulse generated in the beam fuel assembly model. There is a large decrease in the kinetic energy at approximate 5.2 msec. This corresponds to the large loads applied to the rod due to beam-beam contact forces at locations between the spacer grids. These impacts are illustrated in Figure III-69, which show the maximum equivalent plastic strain (EQPS) in the rod cladding as a function of time for three inter-grid locations. A maximum plastic strain of 1.5% is observed between spacer grid locations G and H. A detailed contour plot of this region is presented in Figure III-70.

The plastic strain in the rods at several spacer grid locations is presented in Figure III-71. These strains are approximately an order of magnitude smaller than inter-grid strains. This indicates that the spacer grids contact is much softer than beam-to-beam contact.

Figure III-72 shows the distribution of plastic strains along the length of the rod. The peak equivalent plastic strains are at the inter-rod locations between spacer grids G and H and between grids D and E. Strain at most of spacer grid locations along the rod remain elastic. The maximum plastic strain in the rod at a spacer grid is 0.06% at spacer grid C.

A close examination of the strain distribution in Figure III-74 shows that they are not symmetric about the center of the beam, although the initial beam fuel assembly finite element model and its loading were symmetric. This artifact is a result of the beam contact algorithm in Abaqus. As shown in Figure III-65, the impulses calculated for beam-to-beam contact are only a few microseconds long or roughly equal to three analysis time increments. Since the resolution of the impulse and the analysis time step are of the same order of magnitude, any accumulative numerical error on the position of the beam element nodes may result in a change in the time of contact and therefore the magnitude of the contact force and the subsequent position and velocity of the nodes. This results in a slight asymmetry in the calculated beam forces in the beam fuel assembly model. These forces are subsequently applied to the continuum model and result is the asymmetry of the strain fields shown in Figure III-72.

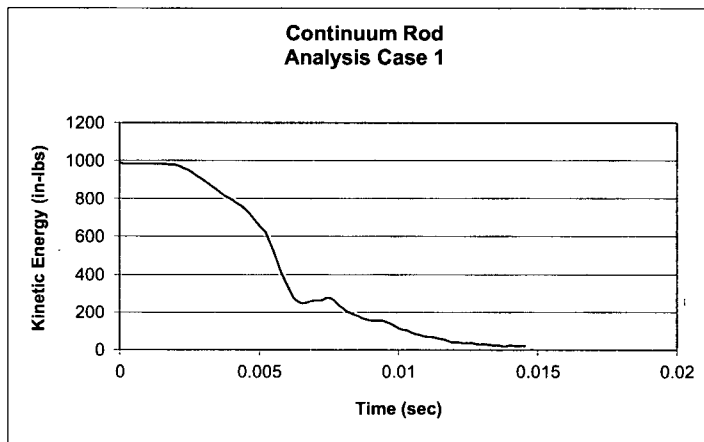


Figure III-68. Kinetic energy for Analysis Case 1

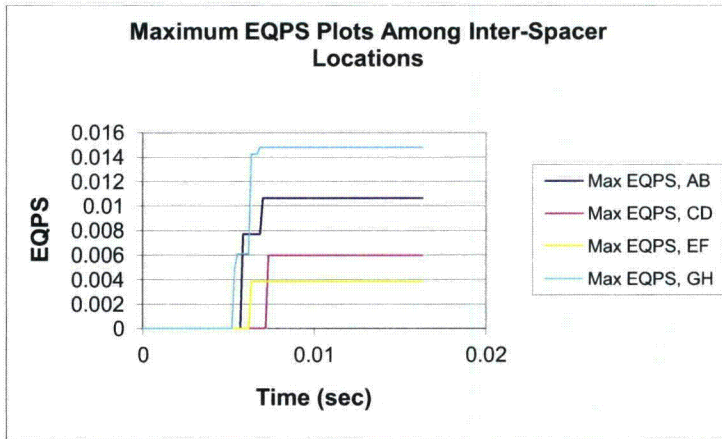


Figure III-69. Maximum equivalent plastic strain versus time for four inter-spacer grid locations. The spacer grids are specified by the letters in the legend (cf. Figure III-74)

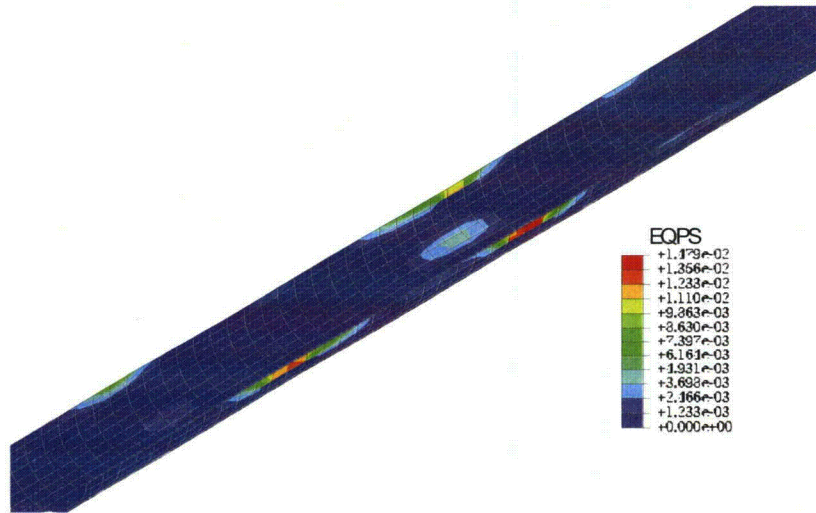


Figure III-70. Maximum equivalent plastic strain field in cladding for Analysis Case 1

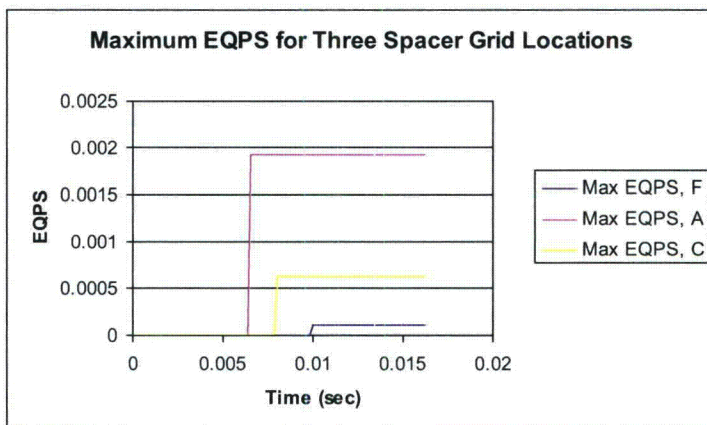


Figure III-71. Maximum equivalent plastic strain versus time for three spacer grid locations The spacer grids are specified by the letters in the legend (cf. Figure III-74).

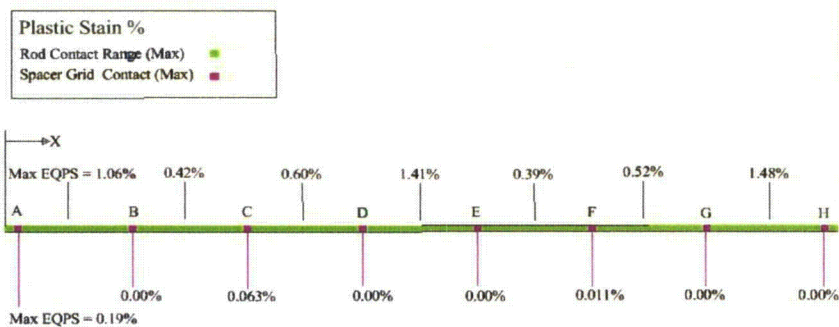


Figure III-72. Schematic showing maximum equivalent plastic strain for spacer grid and inter-spacer-grid locations

Analysis Case 2

For the second analysis case, the Zircaloy material properties remain the same, but the modulus of the UO_2 is decreased by an order of magnitude to provide a probable overestimation of the softness in the post-reactor UO_2 . This softness is engendered by the large cracks that develop in the fuel pellets during its in-core lifetime. The largest plastic strains for this configuration are about one-third higher than those in the previous case of an unirradiated (pristine) UO_2 core. The

maximum EQPS is reached between spacer grids A and B and has a value of 1.98%. A contour plot of this region is presented in Figure III-73, which shows an axial region about 2 inches long with strain between 1% and 2%. The maximum EQPS at four inter-spacer locations as a function of time is shown in Figure III-74 and the maximum EQPS for four spacer grid locations is shown in Figure III-75. These curve are similar in shape to those in Analysis Case 1 where large strains occur at 5.2 msec. For this configuration there are plastic strains in the rod at all but one of the spacer grid locations and the maximum value of plastic strain for a spacer grid location is 0.67% at spacer grid C. A distribution of plastic strain over the entire rod is presented in Figure III-76.

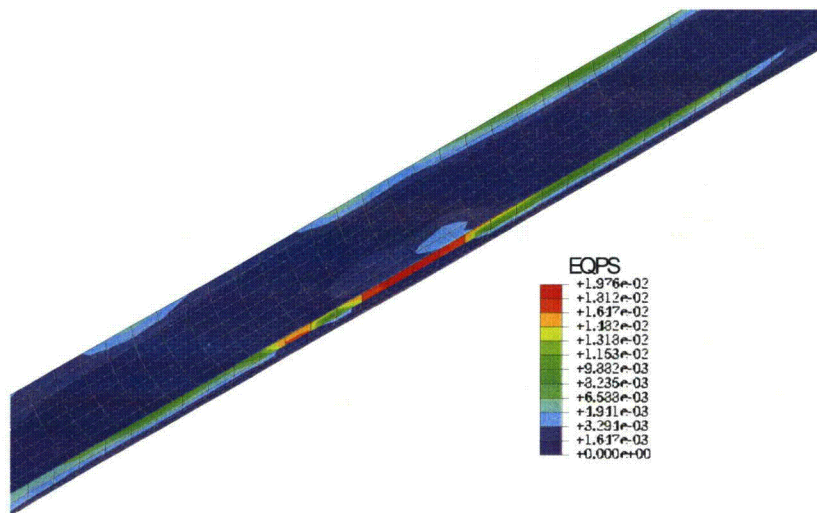


Figure III-73. Maximum equivalent plastic strain field in cladding for Analysis Case 2

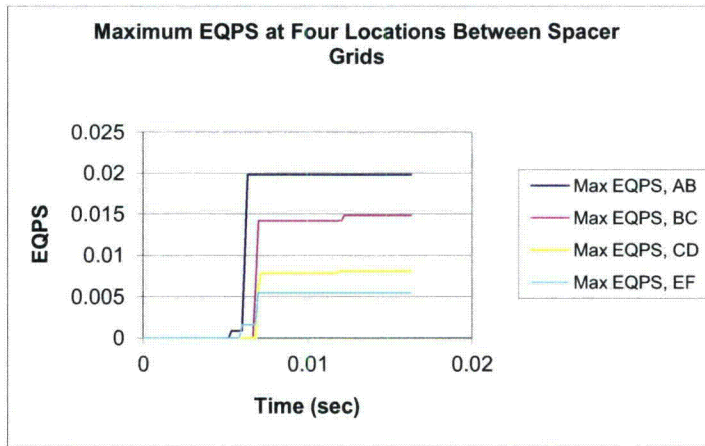


Figure III-74. Maximum equivalent plastic strain versus time for four inter-spacer grid locations. The spacer grids are specified by the letters in the legend (cf. Figure III-78)

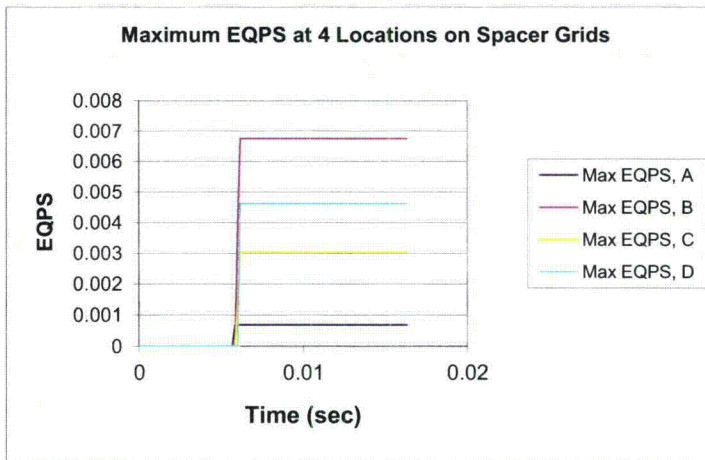


Figure III-75. Maximum equivalent plastic strain versus time for four spacer grid locations. The spacer grids are specified by the letters in the legend (cf. Figure III-78)

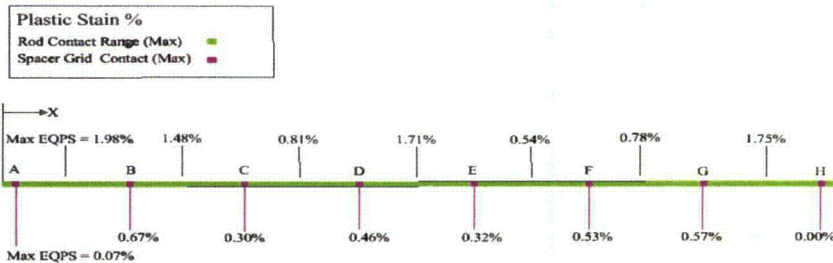


Figure III-76. Schematic showing maximum equivalent plastic strain for spacer grid and inter-spacer-grid locations, Analysis Case 2

III.4.3 Discussion and Conclusions

In this study explicit dynamic finite element analyses of a pressurized water reactor fuel assembly were conducted using two separate finite element models. The first model consisted of structural beam and shell elements and was used to determine the overall response of the complete fuel assembly to a regulatory side impact. Loading data from this analysis was applied to a continuum model of a single fuel pin to determine the localized stress and strain fields. It was observed that during impact the largest loads on the rods were generated from beam-to-beam contact.

Comment [A25]: Should this be Section III.4.4?
Comment [A26]: The argument made in Chapter 3, Sec. 3.6, that since the plastic strain is half the plastic strain capacity of the irradiated rods for 100 g, the rods should not fail at less than 200 g should be developed and discussed in this section.

Due to the lack of experimental data and the variability in properties of stored spent fuel rods, a series of analyses were conducted with variations in the stiffness of the UO₂ core material. A summary of the parameters used in each analysis and the maximum plastic strain calculated in the cladding wall is presented in Table III-8. From Table III-8 it can be concluded that an order of magnitude change in the stiffness of the pellet material results in a 30% increase in the maximum plastic strain in the rod. The materials in this study were modeled as isotropic and homogenous using an elastic plastic power-law hardening model. It is not clear that this approximation accurately models the response of the UO₂ pellets. It is more likely that the initial response would not be a steep linear response as modeled, but would be nonlinear, with a soft initial reaction that would increase in stiffness as the pellet is squeezed. Any attempt to estimate the nonlinear response of the pellet at this point would be pure conjecture.

Table III-8. Analysis Case Summary

Case	Cladding Yield Strength (psi)	UO ₂ Modulus (psi)	Cladding Gap (inches)	Max EQPS (%)
Case 1	65,250	28 x 10 ⁶	None	1.5
Case 2	65,250	28 x 10 ⁵	None	1.96